Aging and Disease
www.aginganddisease.org
Early access date: February 23, 2026
http://dx.doi.org/10.14336/AD.2026.0040

Original Article

Anti-Tumor Immunotherapy of *Scutellaria Baicalensis*-Derived Vesicles on Immune Checkpoint Modulation in Colorectal Cancer

Dianxin Cui[1#], Weilin Qiao[2#], Weixuan Chen[2], Peng Li[1], Shengpeng Wang[1], Fengyun Liao[1], Fei Li[3], Kewei Wang[4], Yitao Wang[1], Huanxing Su[1*], Zhangfeng Zhong[1*]

[1]Macao Centre for Research and Development in Chinese Medicine, Institute of Chinese Medical Sciences, University of Macau, Macao SAR 999078, China. [2]Zhongshan Zhongzhi Pharmaceutical Group Co., Ltd., Zhongshan 528437, China. [3]Department of Urology, Nanfang Hospital, Southern Medical University, Guangzhou, Guangdong 510515, China. [4]Institute of Integrated Traditional Chinese and Western Medicine, Affiliated Hospital of Jiangnan University, Wuxi 214023, Jiangsu, China

[Received January 11, 2026; Revised February 10, 2026; Accepted February 11, 2026]

ABSTRACT: Immune checkpoint blockade (ICB) targeting PD-1/PD-L1 shows promising therapeutic potential in cancer patients. However, the efficacy of its antibody in colorectal cancer remains limited due to the immunosuppressive tumor microenvironment (TME) and related intestinal adverse effects. Plant-derived vesicle (PDV) is emerging natural nanomedicine treating various diseases, especially in cancer therapy. PDV is exhibited with high biocompatibility and low system toxicities, offering a novel strategy to treat colorectal cancer. In this work, we isolated and characterized *Scutellaria baicalensis*-derived vesicles (SBV). SBV exhibited typical vesicular morphology (~104.5 nm) and encapsulated several typical flavonoids, such as baicalin and baicalein, which showed high binding affinity to PD-L1 *in silico*. *In vitro*, SBV inhibited colorectal cancer cell viability and down-regulated the protein expression of PD-L1. Proteomic analysis indicated that SBV regulated multi-pathways including p53 signaling pathway, cell cycle, apoptosis, and endocytosis. *In vivo*, oral administration of SBV markedly suppressed tumor growth in a MC38 xenograft model. Furthermore, SBV down-regulated PD-L1 expression and enhanced tumor immunity with increased $CD3^+/CD8^+$ T cell population and granzyme E (GZME) expression. Notably, the combination treatment of SBV and TOR exhibited synergistic effects in tumor suppression and reduced the colon toxicity induced by Toripalimab (TOR). Our findings suggested SBV serves as a natural nanomedicine with dual potentials, not only could SBV inhibit PD-L1, but also could enhance the systemic anti-tumor immunity in colorectal cancer while reducing the colon toxicity related with PD-1 blockade, providing new insights into the potential application of PDV in cancer immunotherapy.

Keywords: PD-L1, Immunotherapy, Colorectal cancer, *Scutellaria baicalensis*, Huangqin, Plant-derived vesicle

INTRODUCTION

Cancer immunotherapy, particularly the immune checkpoint blockade (ICB), has opened a new horizon in oncology by enhancing the host immune system to kill tumor cells [1]. One of the critical targets in immunosuppression and immune evasion is PD-1/PD-L1. Clinical reports indicated that tumors could induce immunosuppression through the expression of PD-L1 on tumor cells. When the activated T cell expresses PD-1 and binds to PD-L1 on tumor cells, an inhibitory signal is transmitted into the T cell and leads to T cell exhaustion, functional impairment and immune evasion [2-4]. Inhibitors targeting the immune checkpoint such as PD-1/PD-L1 have revolutionized cancer therapy in many solid tumors. However, limited clinical benefit has been

***Correspondence should be addressed to:** Dr. Zhangfeng Zhong (Email: zfzhong@um.edu.mo) and Dr. Huanxing Su (Email: huanxingsu@um.edu.mo), University of Macau, Avenida da Universidade, Taipa, Macao S.A.R., China.

observed in colorectal cancer [5]. According to the NCCN Guidelines (v.2.2025), we have several anti-PD-1/PD-L1 inhibitors recommended into colorectal cancer treatment, including nivolumab, pembrolizumab, cemiplimab, dostarlimab, retifanlimab, toripalimab (TOR) and tislelizumab. The clinical benefit has been observed into a small population of patients (about 15%) with mismatch repair deficiency (dMMR) or microsatellite instability-high (MSI-H) tumors [6]. The limited clinical benefit of ICI therapy in colorectal cancer is largely due to the immunosuppressive tumor microenvironment (TME) that is characteristic of MSS-colorectal cancer. These tumors are considered as "immunologically cold", with poor infiltration of cytotoxic T cells and high burden of immunosuppressive cells, including regulatory T cells (Tregs), myeloid-derived suppressor cells (MDSCs), tumor-associated macrophages (TAMs), and which form a immunosuppressive TME to evade effective treatment [7].

Natural products and herbal medicines are shining resources in tumor drug discovery [8-11]. Accumulating experimental data has appealed to the idea that natural products can regulate immune checkpoints, activate T cell function, and modulate antigen presentation process [12]. More recently, compounds such as Apigenin (from *Matricaria chamomilla*), Arvenin I (from *Cucurbitaceae*), Ursolic acid (from *Crataegus pinnatifida*), and EGCG (from *Camellia sinensis*) have been shown to activate antitumor immunity by modulating the population and cytokine profile of immune cells in TME [13, 14]. Additionally, Benzosceptrin C and 5,7,4′-trimethoxyflavone promote PD-L1 degradation, thereby enhancing immune responses against colorectal cancer [15, 16]. Despite their promise, the clinical application of many natural products is limited by their low bioavailability and non-specific biodistribution, which results in low tumor accumulation and induce higher dosing and further systemic toxicity.

Recently, plant-derived vesicles (PDV) have emerged as promising nanocarriers that can overcome these limitations. PDV are naturally occurring nanoparticles (50-150 nm) secreted by plant cells and possess similar morphological and biophysical characteristics with mammalian vesicles (e.g., lipid bilayer membranes) [17]. PDV possess complicated compositions including various lipids, proteins, miRNAs, and bioactive compounds from their parent plants, endowing PDV with anticancer, anti-inflammatory, and antioxidant activities [18]. In comparison with other synthetic nanoparticles like liposomes or polymer-based nanocarriers, PDV have many obvious advantages, including naturally biocompatible, low immunogenicity, and large-scale production from edible plants with low cost [19]. In addition, accumulating studies demonstrated that PDV could influence tumor immunity. For example, ginger-derived vesicles could enhance immunotherapy in melanoma by specifically interacting with the gut microbiota [20], and vesicles derived from platycodon grandiflorum also affect the microbiota and reversing the immunosuppressive TME [21]. Moreover, garlic-derived vesicles could activate intestinal γδ T cells, thereby remodeling the immune microenvironment to synergize with anti-PD-L1 therapy [22]. In addition, PDV are involved in cross-kingdom communication. The miRNAs and bioactive compounds from Brucea javanica can be uptake by mammalian gut cells and microbiota, which may further modulate the local immune environment around PDV [23]. These studies underscore the translatable potential of specific PDV as targeted therapeutic agents.

Scutellaria baicalensis (Huang Qin, in Chinese), is a highly medicinal herb with anti-inflammatory, antiviral and anticancer activities [24]. Studies have shown that *Scutellaria baicalensis* can modulate host immunity and gut homeostasis, and its extracts demonstrate efficacy against intestinal inflammation and tumors [25, 26]. The major bioactive components of *Scutellaria baicalensis* are flavonoids, such as baicalin and baicalein. These flavonoids exhibit anticancer effects in colorectal cancer models through cell apoptosis, induction cycle arrest, and inhibition of invasion and metastasis [27, 28]. Apart from these cytotoxic effects, recent studies have also revealed marked immunomodulatory effects of both baicalein and baicalin. For instance, baicalein can down-regulate PD-L1 expression on cancer cells [29, 30]. Despite their promising antitumor and immunomodulatory activities, these flavonoids exhibit poor aqueous solubility, rapid metabolism, and low oral bioavailability, which significantly limit their *in vivo* efficacy [31, 32]. In contrast, PDV possesses a natural lipid bilayer structure that improves stability in gastrointestinal conditions and enhances cellular uptake, thereby potentially overcoming these pharmacokinetic limitations. Most recently, our group successfully established the isolation and characterization of *Scutellaria baicalensi*-derived vesicles (SBV) referred to as published patent (CN120384039A): the method could successfully isolate and purify SBV and further demonstrate its anti-tumor activities. We hypothesize that SBV are not just inert carriers but complex, naturally engineered nanovehicles that encapsulate and synergize the bioactive components of *Scutellaria baicalensis*, including baicalin and baicalein. Given the documented anticancer and immuno-modulatory effects of these flavonoids, combined with the inherent advantages of PDV as nanocarriers, we propose that SBV represents a novel, multifaceted therapeutic approach.

This study aims to isolate and characterize SBV, validate their direct interaction with the PD-L1 axis, and demonstrate their efficacy in modulating tumor immunity. We further hypothesize that SBV acts as a natural nanocarrier, delivering anti-tumor components from *Scutellaria baicalensis* to colorectal tumor sites, ultimately establishing SBV as a promising natural immunomodulatory nanomedicine for colorectal cancer therapy.

MATERIALS AND METHODS

Materials

Fresh *Scutellaria baicalensis* was collected from Weifang City, Shandong Province, China. High-purity sucrose was purchased from Aladdin Reagent (Cat# S112228, Shanghai, China). All cell culture reagents were purchased from Gibco (NY, USA), including Penicillin-Streptomycin (10,000 U/mL, Cat# 15140122), 0.25% trypsin-EDTA (Cat# 25200072), fetal bovine serum (FBS, Cat# 26140079), Phosphate buffered saline (PBS, Cat# 10010023), McCoy's 5A Medium (Cat# 16600082), Dulbecco's Modified Eagle Medium (DMEM, Cat# 11995065). DAPI (Cat# C1002), PKH 26 (Cat# C3637S), and sample loading buffer for SDS-PAGE (Cat# P0015L) were purchased from Beyotime Biotech Inc (Shanghai, China). The FITC Phalloidin (Cat# 40735ES75) was purchased from Yeasen Biotechnology (Shanghai, China). The BCA protein assay kit (Cat# 23227) was purchased from Thermo Fisher Scientific Company (MA, USA).

Isolation and purification of plant-derived vesicles

Fresh *Scutellaria baicalensis* was cleaned with deionized ice-water repeatedly and macerated with mechanical blender to get juice. The juice was centrifuged at 1,000 g for 30 min, 5,000 g for 1 h, and 10,000 g for 1 h consecutively to remove debris and fibers. Then, the supernatant was further ultracentrifuged at 200,000 g for 2 h to get exosomal fraction at 4°C. The pellet was resuspended with PBS. When isolating plant-derived vesicles, the resuspended pellet was loaded into a sucrose density gradient with 15%, 30%, 45%, and 60% sucrose solutions and then ultracentrifuged at 200,000 g for another 2 h. SBV was harvested from the interphase between 30% and 45% sucrose layers.

Characterization of SBV

Protein concentration in SBV was measured using the BCA protein assay kit. The particle size distribution was analyzed using Malvern Zetasizer (Model: ZEN5600, UK). The morphology of SBV was captured under TEM (HT7800, Hitachi). SBV was dropped with 10 μL onto a copper grid and then stained with 1% uranyl acetate for one min. Excess stains were washed away and the sample was air-dried ready for observation. The stability of SBV was studied by measuring the change in diameter and zeta potential after SBV were stored at 4°C, 25°C and 37°C for 30 min using the dynamic light scattering (DLS) analysis. Protein profiling of SBV was conducted by using SDS-PAGE. Three batches of SBV, equal amounts of protein (40 μg/well) were then loaded and separated on a 10% SDS-polyacrylamide gel at 80 V (20 min) initially, and then at 120 V (1.5 h) afterwards. The protein was visualized by staining with Coomassie brilliant blue, destaining with deionized water, and then imaging. Total lipids from SBV were extracted following the method below. The SBV was dissolved in a chloroform/methanol (2:1, v/v) mixture. After phase separation, the organic layer was collected, dried with nitrogen, and resuspended in chloroform. For lipid profiling, samples were separated on silica gel thin-layer chromatography (TLC) plates using a chloroform/methanol/acetic acid (190:9:1, v/v/v) solvent mixture as developing agent, and then visualized by spraying the plate with a charring reagent (10% $CuSO_4$ in 8% phosphoric acid) followed by heating at 105°C for 5 min.

Qualitative analysis of phytochemicals

The qualitative analysis of phytochemicals in SBV was conducted by UPLC-Q-TOF/MS. UPLC conditions: Waters Acquity UPLC HSS T3 column (2.1 mm × 100 mm, 1.8 μm); 0.1% phosphoric acid in water (A) and acetonitrile (B); gradient elution (0-4 min, 5-18% B; 4-24 min, 18-35% B; 24-28 min, 35-60% B; 28-30 min, 60-95% B; 30-35 min, 95% B); column temperature: 40°C; injection volume: 2 μL, flow rate: 0.2 mL/min. MS conditions: Electrospray ionization source (ESI), data acquired separately in positive and negative ion modes; primary and secondary mass spectrometry scanning range m/z: 50-1000; ion spray voltage: + 5500/-4500 V; nebulizer gas (GS1): 55 psi; auxiliary heating gas (GS2): 55 psi; collision energy spread (CES): 15 eV; MS2 collision energy: ± 35 eV; declustering potential: ± 80 V; ionization temperature: 500°C; curtain gas: 35 psi.

Quantitative analysis of phytochemicals

HPLC was conducted on a Thermo UltiMate® 3000 HPLC+ system. The chromatographic separation was carried out on an Ultimate C18 column (250 × 4.6 mm, 5 μm particle size). 0.1% Phosphoric acid (A) and Acetonitrile (B). The gradient elution program was as follows: 0-8 min, 5-10% B; 8-15 min, 10-18% B; 15-20

min, 18-20% B; 20-60 min, 20-30% B; 60-80 min, 30-50%B; 80-85 min, 50-95%B; 85-90 min, 95%B; 90-90.1 min, 95-5%B; 90.1-100 min, 5%B. Flow rate: 1.0 mL/min; column temperature: 30°C; wavelength: 274 nm; injection volume: 10 μL.

Molecular docking

Autodock Vina 1.1.2 software was employed to conduct molecular docking and predict the binding affinity of the selected compounds and PD-L1 protein. The three-dimensional structure of PD-L1 (PDB ID: 6PV9) was downloaded from the Protein Data Bank database (http://www.rcsb.org/pdb). Water molecules were removed, hydrogen was added, and the Kollman charge was assigned. A grid box was defined to cover the entire active site. Data processing and image drawing were performed with the lowest energy docking file by PyMOL software.

MTT assay

Cell viability was assessed using the MTT assay. Briefly, HT-29, HCT 116, and MC38 (5×10^3 cells/well) were cultured in 96-well plates and incubated overnight. Then, cells were treated with SBV (0-1000 μg/mL) for 24 h. Following this, 20 μL of MTT solution (5 mg/mL in PBS) was added to each well and incubated at 37°C for 4 h. Next, the culture medium was removed, and 150 μL of DMSO was added to each well to dissolve the formazan crystals. Finally, the absorbance was measured at a wavelength of 490 nm using a microplate reader (SpectraMax iD5, USA). The IC_{50} was calculated using GraphPad Prism software (version 10.1.2).

Western blot

Total protein from HT-29 and HCT 116 cells treated with SBV (0, 50, and 100 μg/mL) for 24 h were extracted using RIPA lysis buffer containing a protease and phosphatase inhibitor cocktail (HY-K0013, MCE, USA). The protein concentration was measured using a BCA protein assay kit (Thermo scientific, USA). For each lane, 40 μg of protein was separated by 10% SDS-PAGE and transferred to a PVDF membrane. The primary antibodies against PD-L1 (1:1000, Cell Signaling Technology, #13684) and GAPDH (1:10000, Cell Signaling Technology, #5174) were incubated with the protein samples overnight at 4°C. The membranes were washed with TBST and then blocked with 5% non-fat milk in TBST for 1 h at room temperature. The primary antibodies were incubated with the protein samples overnight at 4°C. The membranes were washed three times with TBST for 5 min each time and incubated with the corresponding HRP-conjugated secondary antibodies (1:1000, Cell Signaling Technology, #7074) for 1 h at room temperature. Finally, the target protein bands were detected using SuperSignal™ West Femto (Thermo Scientific, USA) and visualized with a chemiluminescence imaging system (Bio-Rad, USA). The density of the target protein bands was measured using ImageJ software (National Institutes of Health, USA).

Flow cytometry

Flow cytometry analysis was conducted to evaluate the effect of SBV on PD-L1 surface expression, following to the manufacturer's protocol with modification. Briefly, HT-29 and HCT 116 cells were treated with SBV in various concentrations of 0, 25, 50, and 100 μg/mL for 24 h. After treatment, cells were harvested and washed with PBS twice and then resuspended in 100 μL PBS (containing 1% BSA). After incubated with APC anti-human PD-L1 antibody (Cat#329708, Biolegend, USA) or the isotype control at 4°C for 30 min, cells were washed and resuspended in cold PBS for flow cytometry analysis.

Cellular Thermal Shift Assay (CETSA)

To investigate the direct interaction between SBV and the PD-L1 protein, a CETSA was performed *in vitro* using cell lysates. Total protein was extracted from HT-29 cells using RIPA lysis buffer containing protease and phosphatase inhibitors. The extracted protein was quantified using a BCA kit. For the binding reaction, the protein lysate was incubated with SBV (100 μg/mL) or an equal volume of PBS (vehicle control) at 4°C for 24 h to allow sufficient interaction. Following incubation, the mixture was aliquoted and subjected to a designated temperature (37, 42, 47, 52, 57, 62, 67, 72, 77, 82 and 87°C) for 3 min, followed by equilibration at room temperature for 5 min. The heat-treated samples were then centrifuged at 120,000 rpm for 20 min at 4°C to pellet the aggregated, denatured proteins. The supernatant containing the soluble protein fraction was carefully collected, mixed with 5× SDS-PAGE loading buffer, and denatured at 95°C for 5 min. The levels of soluble PD-L1 remaining across the temperature gradient were analyzed by Western blot using an anti-PD-L1 antibody (1:1000, Cell Signaling Technology, #13684). GAPDH (1:10000, Cell Signaling Technology, Cat# 5174) was probed as a loading control.

Proteomic analysis

Protein concentration was measured by BCA method. Sample was taken appropriately, and protein denaturation and reductive alkylation was performed; after that trypsin

was added and enzyme digestion was incubated at 37℃ for 2 h. After the end of enzyme digestion, sample was concentrated at 45℃ on C18 column for use; resuspended and detected. Sample was taken appropriately from each group and peptides were chromatographically separated; Buffer: The solution is 0.1 % formic acid aqueous solution; B solution is 0.1 % formic acid acetonitrile aqueous solution (acetonitrile is 80 %). Chromatographic column was balanced with 96 % A liquid. Sample was injected into Trap Column (PepMap Neo Trap, 5 μm, 0.3 × 5 mm, Thermo Scientific, USA) and gradiently separated by the chromatographic analysis column (μPAC Neo High Throughput column, Thermo Scientific, USA). After peptide separation, DIA (data independent acquisition) mass spectrometry was performed with Orbitrap Astral mass spectrometer (Thermo Scientific, USA). Electrospray voltage was 1.9 kV, detection mode was positive ion, parent ion scanning range was 380-980 m/z, first order mass spectrometry resolution was 240000, AGC target was 500%, and first order Maximum IT was 3 ms. Mass spectrometry resolution: 80000, AGC target: 50%, second Maximum IT: 3 ms, RF-lens: 40%, MS2 Activation Type: HCD, Isolation window: 2 Th, Normalized collision energy: 25%, cycle time: 0.6.

Animals and cell lines

C57BL/6J mice (6-8 weeks, male) were purchased from Zhuhai Bestest Biotechnology Co., Ltd. Animal experimental protocols were approved by animal ethics committee of ZHUHAI UM SCIENCE& TECHNOLOGY RESEARCH INSTITUTE (ZUMRI-ERAE-013-2024). HT-29, HCT 116 and MC38 cell lines were obtained from ATCC. HCT 116 and HT-29 cells were cultured in McCoy's 5A medium and MC38 cells were cultured in DMEM. All media were supplemented with 10% (v/v) FBS and 100 IU/mL P/S. Cells were cultured at 37℃, 5% CO_2 in the incubator.

Cellular uptake assay

The assessment of cellular uptake and retention of SBV (5 μg/mL) labeled with PKH 26 (5 μM) was conducted employing advanced imaging and flow cytometry in HT-29 and MC38 cells. HT-29 and MC38 cells were plated at a seeding density of 5 × 10^4 cells per well in confocal dishes. After incubating PKH 26-SBV for appropriate time, cells were counterstained with DAPI for nucleus staining and FITC-Phalloidin for cytoskeletal actin filaments. The colocalization and internalization of SBV in cells were observed under Leica Stellaris 5 spectral confocal system (Leica Camera AG, Germany). To analyze the cellular uptake of PKH 26-SBV at different time intervals, HT-29 and MC38 cells were plated at a seeding density of 5 × 10^4 cells per well in a 6-well plate and treated with PKH 26-SBV for 1, 2, 4 and 6 h. After treatment, the cells were digested with trypsin to digest enzymatically remove or mechanically scrape off from the culture dish to obtain single cell suspension and then washed 3 times with PBS at 4℃. The cellular fluorescence was collected from a flow cytometer (LSRFortessa cytometry, BD biosciences, USA).

In vivo distribution of SBV

To evaluate the biodistribution of SBV *in vivo*, near-infrared fluorescence imaging was performed using the lipophilic dye DIR. SBV were labeled with DIR according to the manufacturer's protocol with minor modifications. Briefly, purified SBV were incubated with 5 μM DIR dye in PBS at 37C for 30 min in the dark. To remove unincorporated free dye, the labeled SBV (SBV-DIR) was subjected to ultrafiltration and washed with PBS. C57 mice (6-8 weeks old, n = 5 per time point) were administered SBV-DIR (equivalent to 10 mg/kg SBV protein) via oral gavage. *In vivo* whole-body fluorescence imaging was conducted at the time point of 0, 3, 6, 9, 12, and 24 h after SBV oral administration. Prior to imaging, mice were anesthetized using 2% isoflurane. Fluorescence signals were captured using the AniView Pro imaging system (BLT Photonics, China). At each point, mice were euthanized, and major organs (spleen, lung, liver, kidney, and heart) as well as the entire gastrointestinal tract (stomach, small intestine, and colon) were excised. These tissues were rinsed gently with PBS to remove surface blood, placed on a black background, and subjected to *ex vivo* fluorescence imaging using the same AniView Pro system with identical settings.

In vivo efficacy evaluation

C57BL/6J mice (6-8 weeks old) were adapted for one week before *in vivo* experiments. After adaptation, MC38 cells (1 × 10^6 cells per mouse) were subcutaneously injected into the right flank of each mouse. The size of the tumor and body weight were measured every three days. When the volume of the tumor reached about 50 mm^3, the mice were randomly assigned into five groups (n = 5 per group): vehicle control group (0 mg/kg SBV, i.g.), SBV (5 mg/kg, i.g.), SBV (10 mg/kg, i.g.), TOR (10 mg/kg, i.p., twice weekly), and SBV (10 mg/kg, i.g.) + TOR (10 mg/kg, i.p., twice weekly). The randomization was based on a computer-generated sequence. Whole animal experiments were performed by researchers blinded to group allocation. TOR is a recommended immunotherapy for the treatment of colorectal cancer following the NCCN guidelines (v2. 2025). The selected dose of SBV were reported in previous publication and further confirmed in

our preliminary experiments [33], while the dose of TOR was following the manufacturer's instruction and previous literature [34] . At the end of 21 days, the mice were sacrificed, and the tumors and organs (kidney, spleen, liver, lung, heart, and colon) were dissected.

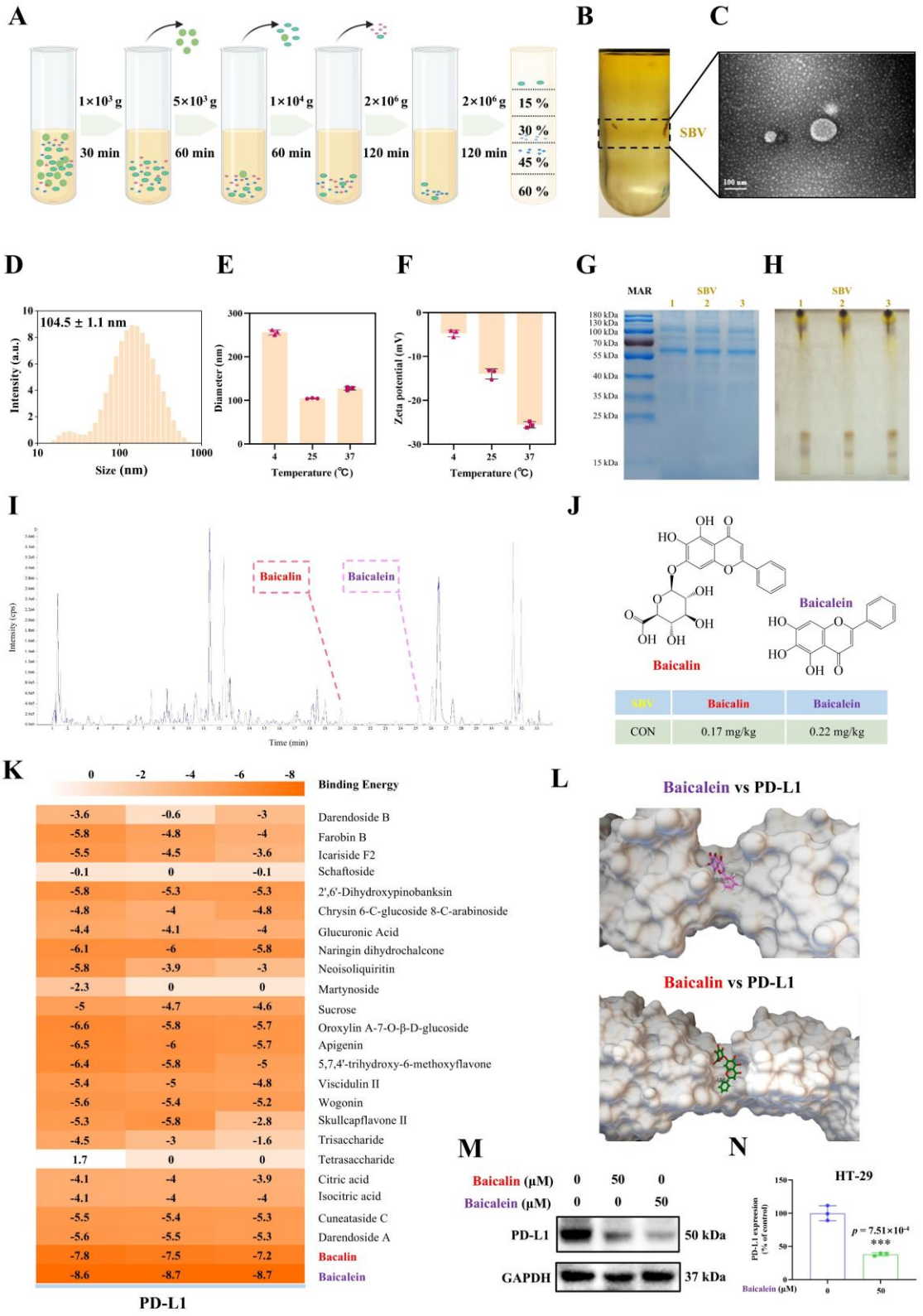

Figure 1. Isolation and comprehensive characterization of SBV. (A) Schematic illustration of SBV isolation and purification via sucrose density gradient ultracentrifugation. **(B)** A representative photograph showing the harvested SBV fraction at the 30-45% sucrose interface. **(C)** TEM image revealing the spherical or cup-shaped morphology of SBV. Scale bar, 100 nm. Dynamic light scattering (DLS) analysis showing the hydrodynamic diameter distribution of SBV in PBS at 25℃ **(D)**, and at different temperatures **(E)**. **(F)** Zeta potential of SBV measured at 4℃, 25℃, and 37℃. **(G)** Protein profile of SBV analyzed by SDS-PAGE and Coomassie brilliant blue staining. **(H)** Thin-layer chromatography (TLC) analysis of lipid components in SBV. **(I)** Base peak chromatogram from UPLC-MS analysis of SBV constituents in positive ion modes. **(J)** Quantitative HPLC analysis of baicalin and baicalein concentrations in SBV. **(K)** Heatmap illustrates the molecular docking binding energies between 25 identified SBV compounds and the PD-L1 protein. **(L)** Three-dimensional representation of the molecular docking poses of baicalein and baicalin within the PD-L1 binding pocket. **(M)** PD-L1 expression in HT-29 cells treated with baicalin (50 μM), baicalein (50 μM), or DMSO (control) for 24 h. **(N)** Significant inhibitory effect of baicalein on PD-L1 expression. Data was shown as mean ± SD (n = 3). The normality of data were assessed using the Shapiro-Wilk test. Statistical significance between groups was determined by unpaired Student's t-test. ***$p < 0.001$ vs. control group.

Histological staining

The colon, spleen, liver, lung, kidney, and heart tissues were dissected from the mice and fixed in 4% paraformaldehyde. After fixation, the tissues were dehydrated and embedded in paraffin. Thin slices were cut from the paraffin-embedded sections and stained with hematoxylin and eosin (H&E) for histological imaging (DS-RI2, Nikon). Representative images were selected across different fields to reflect typical observations.

Statistical analysis

Quantitative data were shown as mean ± standard deviation (SD) or mean ± standard error mean (SEM). Normality of data distribution was assessed using the Shapiro-Wilk test. For comparison between two groups, the unpaired two-tailed Student's T-test was employed. For comparisons between three or more groups, one-way ANOVA followed by Dunnett's test was applied. When data was not met normality, the Kruskal-Wallis test followed by Dunn's multiple comparisons test was performed. $p < 0.05$ was considered significantly different. All statistical analysis was performed using GraphPad Prism software (version 10.1.2).

RESULTS

Isolation and characterization of SBV

SBV was isolated from fresh *Scutellaria baicalensis* juice and purified through sucrose gradient ultracentrifugation. Vesicles were enriched at the 30-45% (w/v) sucrose interface; this fraction was collected for further analyses (Fig. 1A and 1B). TEM image revealed that SBV exhibited typical vesicle morphology, appearing as spherical or cup-shaped structures bounded by a bilayer membrane (Fig. 1C). DLS measurements in PBS showed an average particle size of 104.5 ± 1.1 nm at 25℃ (Fig. 1D). The average size was 256.0 ± 5.6 nm at 4℃ and 127.5 ± 3.6 nm at 37℃ (Fig. 1E). Zeta potential values were -4.7 ± 0.8 mV at 4℃, -14.0 ± 1.2 mV at 25℃, and -25.6 ± 0.7 mV at 37℃ (Fig. 1F). Protein content analysis by Coomassie brilliant blue staining indicated that most SBV-associated proteins had molecular weights between 55-100 kDa (Fig. 1G). Thin-layer chromatography (TLC) revealed the presence of diverse lipids in SBV (Fig. 1H). Chemical profiling using UPLC-MS in positive and negative ionization modes totally identified 25 bioactive constituents, primarily flavonoids, organic acids, and glycosides (Fig. 1I and Table 1). Quantitative analysis showed that the concentrations of the anticancer compounds baicalin and baicalein were 0.17 mg/kg and 0.22 mg/kg, respectively (Fig. 1J). Molecular docking of all 25 identified compounds with PD-L1 protein revealed favorable binding energies for several constituents, as illustrated in the docking energy heatmap (Fig. 1K). Notably, both baicalin and baicalein demonstrated a strong binding affinity for PD-L1, with binding energies lower than -7 kJ/mol (Fig. 1L). To further validate these *in silico* predictions, we evaluated the effects of baicalin and baicalein on PD-L1 expression. Consistent with *in silico* predictions, both flavonoids (50 μM) reduced PD-L1 protein expression in HT-29 cells, with baicalein showing superior inhibitory effect (Fig. 1M and 1N).

Inhibitory effect of SBV on cell viability and PD-L1 protein expression *in vitro*

To assess the anti-tumor potential of SBV, we first performed an MTT assay. SBV inhibited the viability of HCT 116, HT-29, and MC38 colorectal cancer cells in a dose-dependent manner, with IC_{50} values of 103.8 ± 21.9 μg/mL, 94.2 ± 21.8 μg/mL, and 84.3 ± 24.2 μg/mL (Fig. 2A). Furthermore, we investigated the effect of SBV on PD-L1 protein expression. Western blot analysis revealed that treatment with SBV (50 and 100 μg/mL) significantly reduced PD-L1 protein expression in both HCT 116 (Fig. 2B and 2C) and HT-29 (Fig. 2D and 2E) cells. This effect was further confirmed by flow cytometry, which showed a marked decrease in PD-L1 expression in HCT 116 (Fig. 2F and 2G) and HT-29 (Fig. 2H and 2I) cell lines

following treatment with 25, 50, and 100 μg/mL SBV. To further confirm the observed PD-L1 downregulation involved direct target binding, we employed a CETSA experiment. Analysis of PD-L1 thermal stability in HT-29 cell lysates revealed a distinct protective effect. The results demonstrated that SBV treatment significantly increased the thermal stability of PD-L1 protein, confirming their direct interaction (Fig. 2J and 2K).

Table 1. Putative identification of phytochemicals in SBV using UPLC-MS/MS under positive and negative ionization modes.

NO.	RT (min)	Formula	MS1-POS	ppm	MS2-POS	MS1-NEG	ppm	MS2-NEG	Identification
1	1.205	$C_6H_{10}O_7$	-	-	-	193.0361	3.7	55.0195,59.0145,71.0144,72.9940,85.0300,89.0247,95.0140,101.0249,113.0253	Glucuronic Acid
2	1.337	$C_{12}H_{22}O_{11}$	365.1065	2.9	185.0425,203.0535	377.0863	1.8	59.0139,89.0248,119.0351,161.0456,179.0568,215.0332,341.1103	Sucrose or isomer
3	1.337	$C_{18}H_{32}O_{16}$	527.1596	2.6	347.0950,365.1052	539.1391	1.2	89.0243,161.0457,179.0571,221.0676,377.0862,503.1646	Trisaccharide
4	1.337	$C_{24}H_{42}O_{21}$	689.2125	2.1	527.1569	701.1934	3.1	179.0568,383.1213,665.2203	Tetrasaccharide
5	1.534	$C_6H_8O_7$	215.0175	5.9	-	191.0204	3.5	57.0350,67.0195,85.0301,87.0092,111.0095	Citric acid
6	1.863	$C_6H_8O_7$	215.0171	4.1	-	191.0205	4.1	57.0347,67.0191,85.0299,87.0092,111.0091	Isocitric acid
7	6.495	$C_{19}H_{28}O_{12}$	471.1484	2.3	-	447.1511	0.7	59.0144,89.0249,99.0093,113.0249,135.0460,149.0462,161.0461,191.0573,315.1105	Cuneataside C or isomer
8	7.524	$C_{19}H_{28}O_{11}$	455.1546	4.9	317.0853,321.1098	431.1566	1.7	59.0145,71.0143,89.0252,99.0095,113.0251,119.0436,149.0467,161.0461,191.0579,299.1154	Darendoside A
9	8.36	$C_{21}H_{20}O_{12}$	465.1037	2	303.0498	463.0893	2.4	125.0251,151.0048,175.0046,283.0267,301.0372	Carthamidin-7-O-β-D-glucuronide
10	8.548	$C_{21}H_{32}O_{12}$	499.1791	1	353.1207	475.1825	0.8	59.0143,71.0141,85.0300,89.0248,113.0251,119.0353,161.0461,329.1247	Darendoside B
11	8.794	$C_{27}H_{30}O_{14}$	-	-	-	577.1574	1.9	267.0674,295.0631,457.1160	Farobin B or isomer
12	8.836	$C_{18}H_{26}O_{10}$	425.1419	0.2	293.0984	401.1459	1.4	59.0139,71.0140,73.0296,85.0295,99.0083,101.0248,113.0246,159.0305,161.0461,269.1044	Icariside F2 or isomer
13	9.714	$C_{26}H_{28}O_{14}$	565.1546	-1	295.0596,307.0591,325.0699,337.0698,379.0803,397.0912,427.1011,457.1099,469.1120,481.1120,511.1229,529.1329,547.1449	563.1424	3.1	353.0691,383.0801,443.1011,473.1115	Schaftoside or isomer
14	9.888	$C_{15}H_{12}O_7$	305.0669	4.3	123.0436,149.0228,153.0182,191.0327,259.0594	303.0524	4.5	57.0351,123.0458,125.0256,149.0257,177.0207,217.0521	2',6'-Dihydroxypinobanksin
15	10.452	$C_{26}H_{30}O_{14}$	567.1717	1.5	105.0328,147.0433,219.0281,261.0395,291.0500,309.0619,315.0484,363.0795,393.0878,411.0987,429.1143,465.1159,495.1261,531.1475,549.1584	565.1582	3.4	167.0360,209.0473,239.0575,269.0683,299.0790,329.0899,355.0840,385.0951,419.1216,445.1161,475.1267	naringenin 8-C-arabinoside 7-O-glucoside or isomer
16	11.122	$C_{26}H_{28}O_{13}$	549.1617	2.6	279.0648,291.0624,309.0752,321.0761,333.0759,339.0864,345.0760,363.0860,375.0851,381.0961,393.0963,405.0964,411.1065,417.0962,429.1053,441.1133,45	547.1468	2	281.0826,309.0781,337.0732,349.0729,367.0840,427.1048,457.1157,487.1257	Chrysin 6-C-glucoside 8-C-arabinoside or isomer

					3.1155,465.1167,477.1165,483.1264,495.1284,513.1375,531.1486				
17	11.377	$C_{26}H_{28}O_{13}$	549.1617	2.6	279.0658,309.0762,321.0758,333.0764,363.0865,375.0865,393.0970,411.1083,465.1180,483.1287,495.1290,513.1384,531.1490	547.1478	3.8	281.0838,309.0784,337.0741,367.0848,397.0949,409.0950,427.1058,457.1167,487.1273,529.1391	Chrysin 6-C-glucoside 8-C-arabinoside or isomer
18	11.868	$C_{26}H_{28}O_{13}$	549.1606	0.6	279.0632,291.0636,309.0751,321.0750,333.0752,363.0854,375.0846,393.0966,411.1064,465.1145,483.1288,495.1280,513.1377,531.1485,549.1593	547.1471	2.5	281.0822,337.0733,349.0730,367.0843,409.0943,427.1053,457.1158,487.1263	Chrysin 6-C-glucoside 8-C-arabinoside or isomer
19	12.314	$C_{26}H_{28}O_{13}$	549.1623	3.7	279.0657,291.0657,309.0762,321.0767,333.0765,363.0970,375.0866,381.0970,393.0971,411.1066,417.0968,441.1153,453.1175,477.1179,483.1290,495.1283,513.1385,531.1487	547.1462	0.9	281.0831,309.0787,337.0738,349.0741,367.0846,379.0841,397.0948,427.1055,457.1169,529.1379	Chrysin 6-C-glucoside 8-C-arabinoside or isomer
20	12.697	$C_{27}H_{34}O_{14}$	605.1857	2.7	443.1304	581.1896	3.5	167.0358,257.0832,299.0951,329.1049,461.1483,491.1593,563.1800	Naringin dihydrochalcone or isomer
21	12.71	$C_{26}H_{28}O_{13}$	549.1612	1.7	309.0755,321.075,363.0860,375.0857,381.0977,393.0959,429.1159,441.1163,453.1179,465.1163,477.1167,495.1281,513.1397,531.1510	547.1475	3.3	337.0743,367.0846,427.1064,457.1168	Chrysin 6-C-glucoside 8-C-arabinoside or isomer
22	12.898	$C_{26}H_{28}O_{13}$	549.1619	3	279.0646,291.0645,309.0740,321.0746,333.0738,363.0857,375.0851,381.0960,393.0949,411.1043,417.0961,435.1060,453.1153,465.1160,495.1279,531.1492	547.1467	1.8	-	Chrysin 6-C-glucoside 8-C-arabinoside or isomer
23	13.306	$C_{23}H_{24}O_{12}$	493.1344	0.7	331.082	491.1213	3.7	299.0213,314.0445,329.0686	5,2'-dihydroxy-7,8-dimethoxyflavone-6'- O-β-D-glucoside or isomer
24	14.057	$C_{21}H_{20}O_{9}$	417.1188	1.9	267.0645,297.0755,381.0963,399.1071	415.1044	2.3	267.0678,295.0629	Chrysin-6/8-C-glucoside
25	14.402	$C_{34}H_{36}O_{17}$	717.2039	1.9	423.1071,585.1578	715.1911	4.4	257.0469,403.0848	Unknown
26	18.097	$C_{21}H_{22}O_{9}$	441.1169	2.9	185.0411,203.0527,261.0521,279.0635	417.1203	2.9	211.0783,255.0680	Neoisoliquiritin or isomer
27	18.419	$C_{31}H_{40}O_{15}$	670.2711	0.8	145.0276,177.0547,323.1111,339.1083,485.1645	651.2339	6.8	160.0179,175.0421	Martynoside or isomer
28	18.958	$C_{22}H_{22}O_{10}$	469.1108	0.6	291.0264,307.0573	445.1141	0.2	239.0360,267.0314,268.0388,283.0626,430.0913	Oroxylin A-7-O-β-D-glucoside
29	20.039	$C_{21}H_{18}O_{11}$	447.0938	3.6	271.061	445.0787	2.4	269.0476	Baicalin
30	25.2	$C_{15}H_{10}O_{5}$	271.0614	4.8	95.0134,103.0547,123.0084,169.0141,225.0555,253.0511	269.0464	3.2	65.0037,136.9887,139.0045,169.0669,171.0462,195.0468,197.0623,223.0420	Baicalein
31	26.036	$C_{16}H_{12}O_{6}$	301.0724	5.8	156.0057,184.0011,286.0483	299.0575	4.6	125.9962,153.9918,171.0458,181.9867,284.0348	5,7,4'-trihydroxy-6-methoxyflavone or isomer
32	26.448	$C_{15}H_{10}O_{5}$	271.0617	5.9	103.0538,105.0329,123.0073,129.0336,141.0687,169.0131	269.0462	2.4	169.0663,171.0460,197.0619,213.0567,225.0568	Apigenin
33	27.375	$C_{17}H_{14}O_{7}$	331.0833	6.3	154.9974,180.0052,182.9929,298.0485,301.0352,316.0591	329.068	4	143.0511,171.0455,183.0462,199.0411,215.0360,227.0363,243.031	Viscidulin II

								1,271.0266,299.0221,314.0453	
34	31.408	$C_{16}H_{12}O_5$	285.0772	5.1	151.0544,179.0493,242.0579,252.0422,269.0447,270.0567	283.0625	4.6	110.0017,163.0049,239.0364,268.0418	Wogonin
35	31.815	$C_{19}H_{18}O_8$	375.1087	3.3	169.0128,197.0083,227.0553,327.0509,345.0614,360.0846	373.094	3	194.9944,285.0055,300.0297,328.0248,343.0482,358.0713	Skullcapflavone II
36	31.938	$C_{16}H_{12}O_5$	285.077	4.4	140.0104,168.0055,270.0559	283.0618	2.1	110.0019,165.9917,268.0395	Oroxylin A

Global proteomic alterations in HT-29 cells treated with SBV

To investigate the molecular mechanisms underlying the biological effects of SBV, we conducted a comprehensive, quantitative proteomic analysis of HT-29 cells treated with SBV. Principal component analysis (PCA) showed clear separation between the SBV-treated and control groups, with the first principal component (PC1) explaining 84.3% of the total variance (Fig. 3A). A volcano plot identified 2,601 differentially expressed proteins (DEPs) based on the thresholds of |Fold Change| > 1.2 and $p < 0.05$, of which 1,756 were upregulated and 845 downregulated (Fig. 3B). Unsupervised hierarchical clustering confirmed consistent expression patterns of these DEPs in response to SBV treatment (Fig. 3C). KEGG pathway enrichment analysis revealed significant alterations in several cancer-related pathways, including the p53 signaling pathway, endocytosis, cell cycle regulation, and apoptosis (Fig. 3D). Gene Ontology (GO) enrichment analysis further highlighted immune-related terms, such as “T cell receptor binding”, “positive regulation of activated CD8-positive T cells,” and “positive regulation of T cell-mediated immunity” (Fig. 3E). To find out key DEPs involved in these pathways, we focused on proteins associated with the p53 signaling pathway (PIG3 and ATM), endocytosis (ARRB2), and pro-apoptotic (BAD) related proteins were significantly upregulated. In addition, cell cycle (CDK1 and Cyclin B1), immune modulation (PD-L1, STAT3, and IFNGR1), and anti-apoptotic (MCL1) related proteins were significantly downregulated (Fig. 3F).

Cellular uptake of SBV *in vitro*

We evaluated the internalization of SBV by colorectal cancer cells using confocal microscopy and flow cytometry. SBV was labeled with the lipophilic dye PKH 26 and incubated with MC38 (Fig. 4A) and HT-29 cells (Fig. 4B) for 1, 2, 4, and 6 h. Confocal microscopy images revealed time-dependent cellular uptake, with faint membrane-associated fluorescence at 1 h that intensified and localized to the perinuclear region by 2-4 h, and widespread cytoplasmic distribution by 6 h. Flow cytometry quantitatively confirmed these observations: the uptake rate of SBV by MC38 cells increased from 18.2% at 1 h to 97.8% at 6 h (Fig. 4C and 4D), while HT-29 cells showed an increase from 2.1% to 77.5% over the same period (Fig. 4E and 4F).

Biodistribution and biocompatibility assessment of SBV

To investigate the gastrointestinal fate and systemic biodistribution of orally administered SBV, we performed near-infrared fluorescence imaging. Following a single oral gavage of DIR-labeled SBV (SBV-DIR), whole-body fluorescence signals were monitored over 24 h (Fig. 5A). At the early time points (3 and 6 h), fluorescence was predominantly localized within the abdominal region, specifically the gastrointestinal tract. The signal intensity in this area peaked at around 6-9 h post-administration and subsequently diminished by 24 h, indicating the transit and clearance of SBV. Notably, no significant fluorescence accumulation was observed in other major body cavities throughout the observation period, suggesting minimal systemic absorption. To quantitatively assess organ-specific accumulation, we performed *ex vivo* imaging on harvested tissues. Consistent with the *in vivo* observations, the strongest fluorescence signals were detected in the gastrointestinal organs, including the stomach, small intestine, and colon. Given the oral administration route, we next evaluated the colloidal stability of SBV in simulated gastrointestinal fluids. Incubation in artificial gastric juice (AGJ), artificial intestinal fluid (AIF), or a mixture of both (AGJ + AIF) for 2 h did not induce aggregation or significant degradation. DLS showed that the particle size distribution and zeta potential of SBV remained largely unchanged, with non-significant increase observed in AGJ (Fig. 5B and 5C). In addition, we assessed the hemocompatibility of SBV as a preliminary safety evaluation for potential systemic exposure. Incubation of SBV at concentrations ranging from 31.25 to 1000 μg/mL with a 2% red blood cell suspension for 1 h resulted in hemolysis rates consistently below 2% at all tested doses (Fig. 5D).

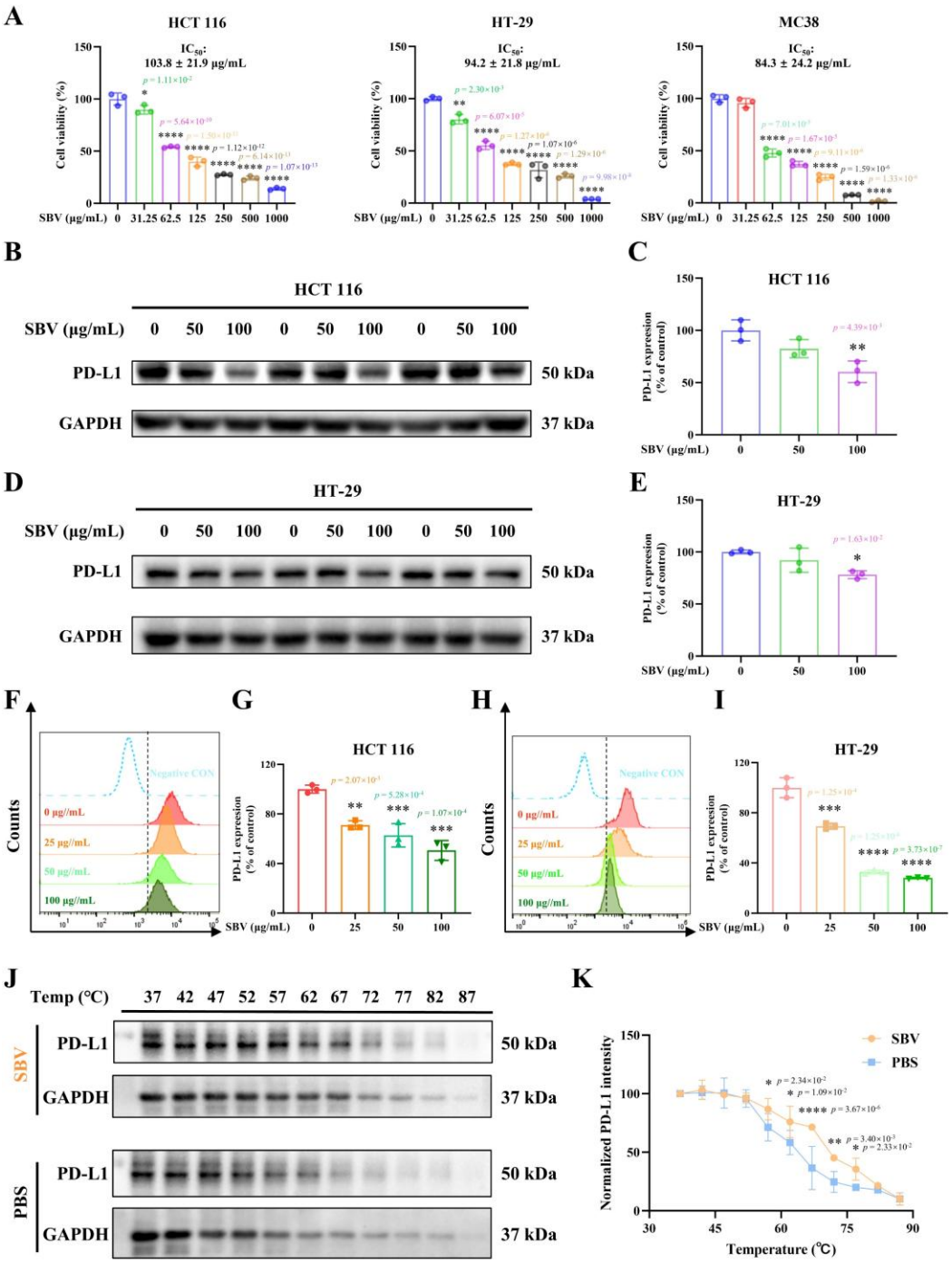

Figure 2. SBV inhibited colorectal cancer cell viability and downregulated PD-L1 expression *in vitro*. (A) Dose-response curves of HCT 116, HT-29, and MC38 cells treated with SBV for 24 h assessed by MTT assay. IC_{50} were shown as mean ± SD. **(B, C)** Western blot analysis and quantification of PD-L1 protein expression in HCT 116 cells treated with SBV (50 and 100 μg/mL) for 24 h. **(D, E)** Western blot analysis and quantification of PD-L1 expression in HT-29 cells treated with SBV for 24 h. **(F, G)** Flow cytometry analysis and statistical summary of cell surface PD-L1 expression in HCT 116 treated with indicated concentrations of SBV. **(H, I)** Flow cytometry analysis and statistical summary of cell surface PD-L1 expression in HT-29 treated with indicated concentrations of SBV, data were shown as mean ± SEM (n = 3). **(J)** Cellular thermal stability of PD-L1 in HT-29 cell lysates incubated with SBV (100 μg/mL) or PBS (control) across the temperature gradient of 37-87°C. **(K)** Quantification of PD-L1 thermal stability modulated by SBV, data were shown as mean ± SD (n = 3). Normality was assessed using the Shapiro-Wilk test. Statistical significance was determined by one-way ANOVA followed by Dunnett's test for (A, C, E, G, and I) or unpaired Student's t-test for (K). *$p < 0.05$, **$p < 0.01$, ***$p < 0.001$, and ****$p < 0.0001$ vs. control group.

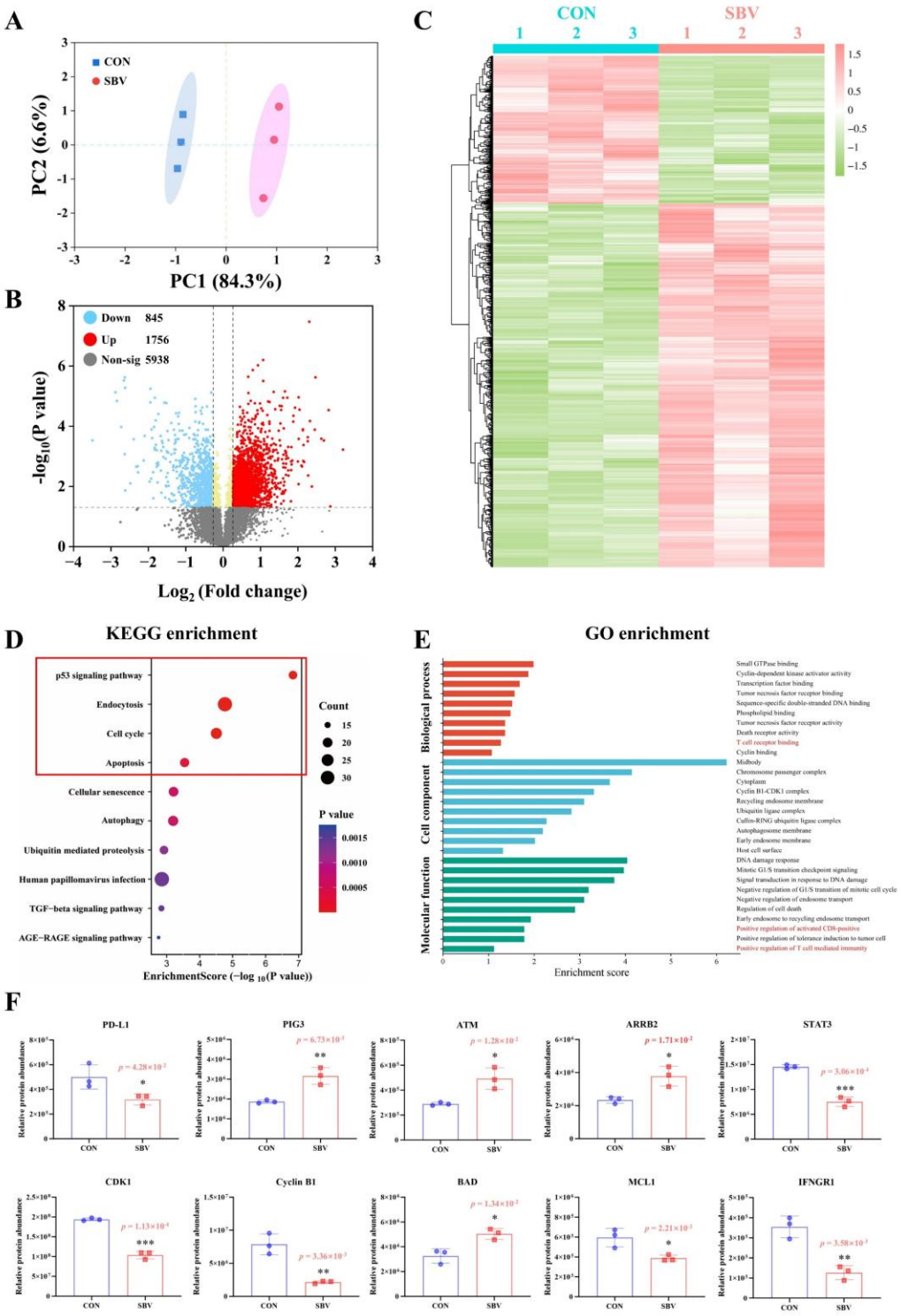

Figure 3. Global proteomic profiling of HT-29 cells treated with SBV. (A) Principal component analysis (PCA) score plot showing separation of control and SBV-treated groups. **(B)** Volcano plot of differential expression proteins (DEPs). Red dots represent 1756 upregulated proteins, blue dots represent 845 downregulated proteins (|Fold Change| > 1.2, $p < 0.05$). **(C)** Heatmap of hierarchical cluster analysis of all DEPs. **(D)** KEGG pathway enrichment analysis of the DEPs. **(E)** GO enrichment analysis of biological process, cell component and molecular function. **(F)** Key DEPs involved in p53 signaling, endocytosis, cell cycle, apoptosis, and immune checkpoint related pathways. Data were shown as mean ± SD (n = 3). The normality of data was assessed using the Shapiro-Wilk test. Statistical significance between groups was determined by unpaired Student's t-test. *$p < 0.05$, **$p < 0.01$, and ***$p < 0.001$ vs. control group.

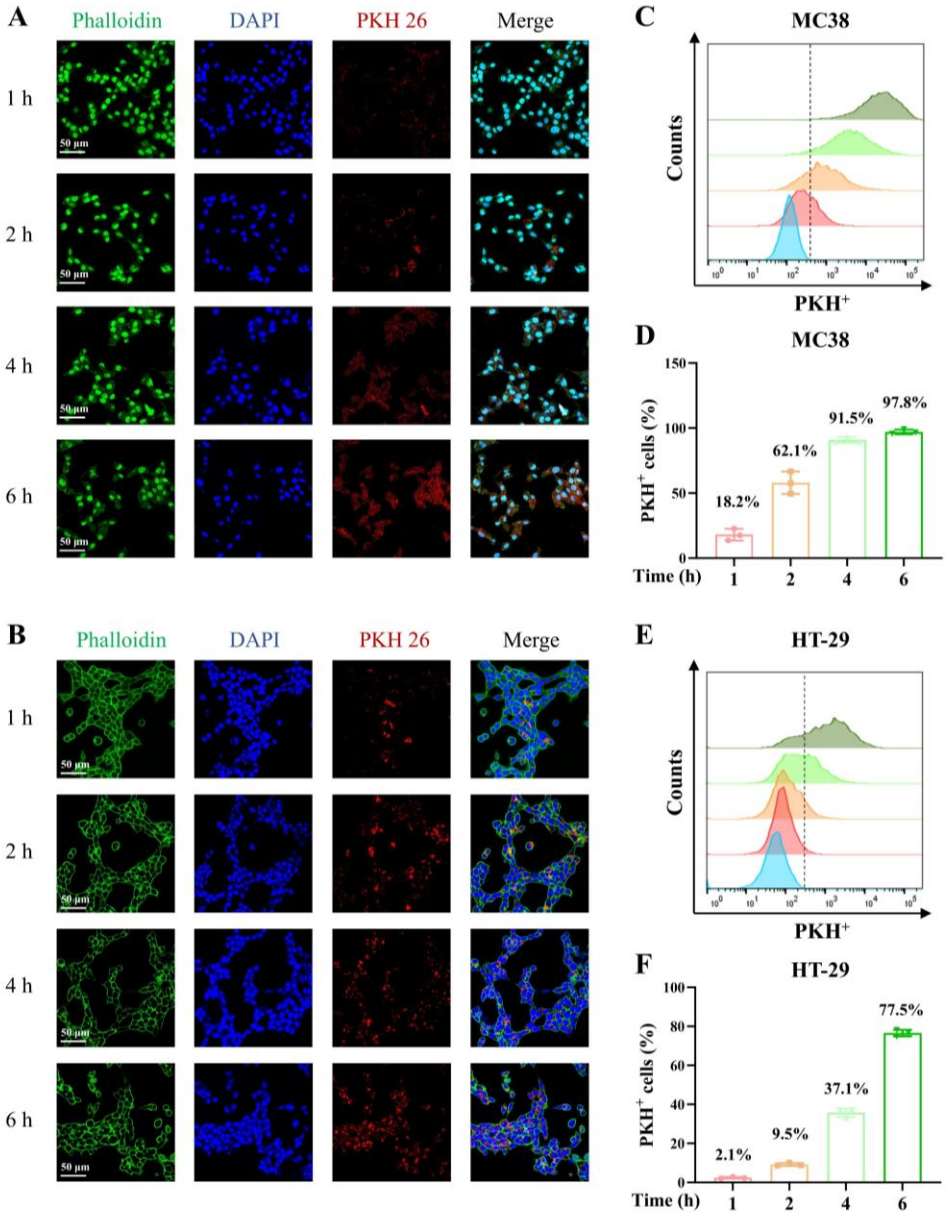

Figure 4. Cellular uptake kinetics of SBV in colorectal cancer cells. Confocal microscopy images showing the time-dependent internalization of PKH 26-labeled SBV (red) in MC38 **(A)** and HT-29 **(B)** cells. Cell nuclei and F-actin were stained with DAPI (blue) and phalloidin (green), respectively. Scale bar, 50 μm. **(C, D)** Flow cytometry analysis and quantification of PKH 26^+ MC38 cells at different time points. **(E, F)** Flow cytometry analysis and quantification of PKH 26^+ HT-29 cells at different time points. Representative images were selected from at least three independent experiments and data were presented as mean ± SEM (n = 3).

Anti-tumor efficiency of SBV *in vivo*

Given the promising *in vitro* results, we evaluated the therapeutic potential of SBV in an MC38 xenograft mouse model. Tumor-bearing mice were randomized into five groups: vehicle control [SBV (0 mg/kg)], SBV (5 mg/kg), SBV (10 mg/kg), TOR (10 mg/kg), and combination therapy [SBV (10 mg/kg) + TOR (10 mg/kg)]. Treatments were administered for 21 days according to the schedule in Fig. 6A. Representative photographs of excised tumors showed visible reduction in tumor size in the SBV (10 mg/kg), TOR, and combination groups compared to control (Fig. 6B). All groups kept body weights stable during the whole study, showing good tolerability (Fig. 6C). Tumor growth curves indicated that SBV attenuated tumor progression in a dose-dependent manner, with SBV

(10 mg/kg) exhibited stronger inhibitory effect than SBV (5 mg/kg). TOR monotherapy also tangibly inhibited tumor growth, and the combination therapy led to the most intense restraint, suggesting a potentially combined effect (Fig. 6D). The final tumor weight measurement confirmed these findings: the SBV (10 mg/kg) group had considerably less tumor weight than the control group, and the combination group presented the most significant reduction (Fig. 6E). Flow cytometry demonstrated that SBV (10 mg/kg) significantly raised the amount of $CD3^+$ T cells and $CD8^+$ cytotoxic T cells in splenic lymphocytes (Fig. 6F).

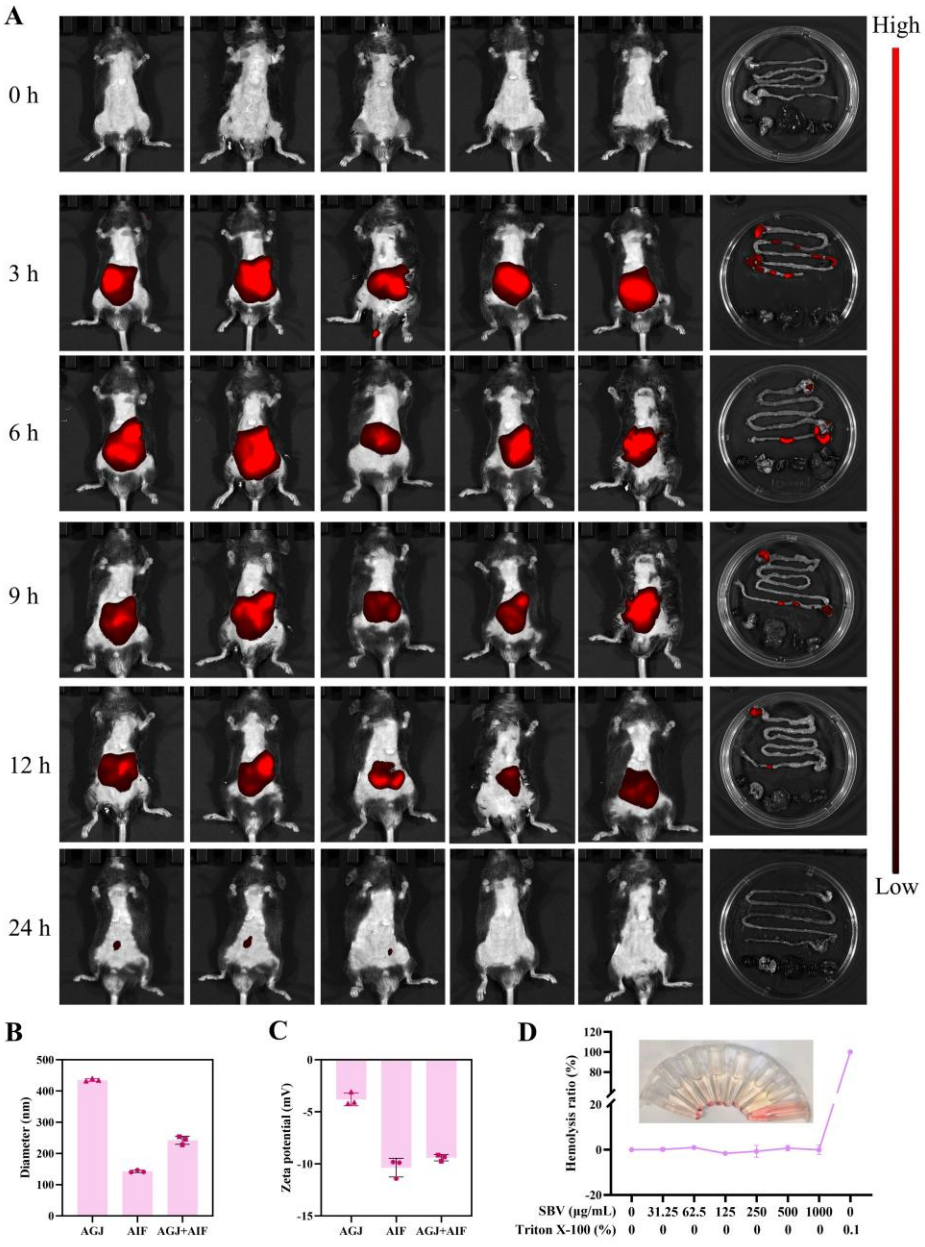

Figure 5. *In vivo* biodistribution, gastrointestinal stability, and hemocompatibility of SBV. (A) Near-infrared fluorescence imaging of mice (n = 5) following a single oral gavage of DIR-labeled SBV (SBV-DIR), and *ex vivo* fluorescence imaging of major organs and the gastrointestinal tract harvested at indicated time point. DLS analysis of SBV particle size **(B)** and zeta potential **(C)** after 1 h incubation in artificial gastric juice (AGJ), artificial intestinal fluid (AIF), or a mixture (AGJ + AIF). **(D)** Hemolysis assay of SBV (31.25-1000 μg/mL) incubated with red blood cell suspension, data were presented as mean ± SD (n = 3).

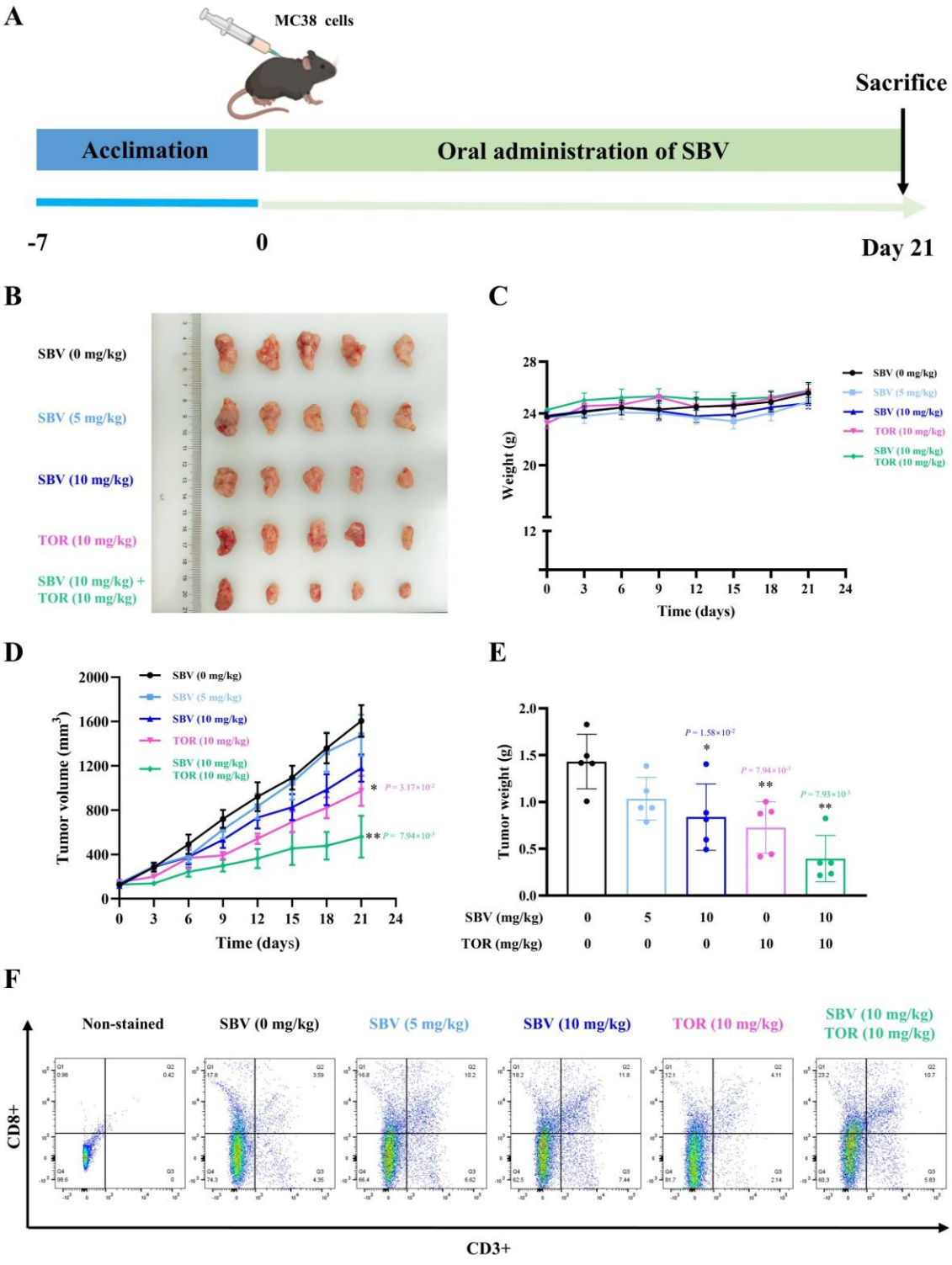

Figure 6. ***In vivo*** **antitumor effect of SBV in MC38 syngeneic mouse model. (A)** Experimental timeline and schedule of whole treatment. **(B)** Representative images of excised tumors from each group at the end point. **(C)** Body weight changes of mice during the 21-day treatment period. **(D)** Tumor growth curves for each group. **(E)** Final tumor weight of each group. **(F)** Flow cytometric analysis of $CD3^+$ and $CD8^+$ T cell population in splenic lymphocytes. Statistical significance was determined using non-parametric tests followed by Kruskal-Wallis with Dunn's multiple comparisons test. Data were mean ± SD (n = 5). * $p < 0.05$ and ** $p < 0.01$ vs. control group.

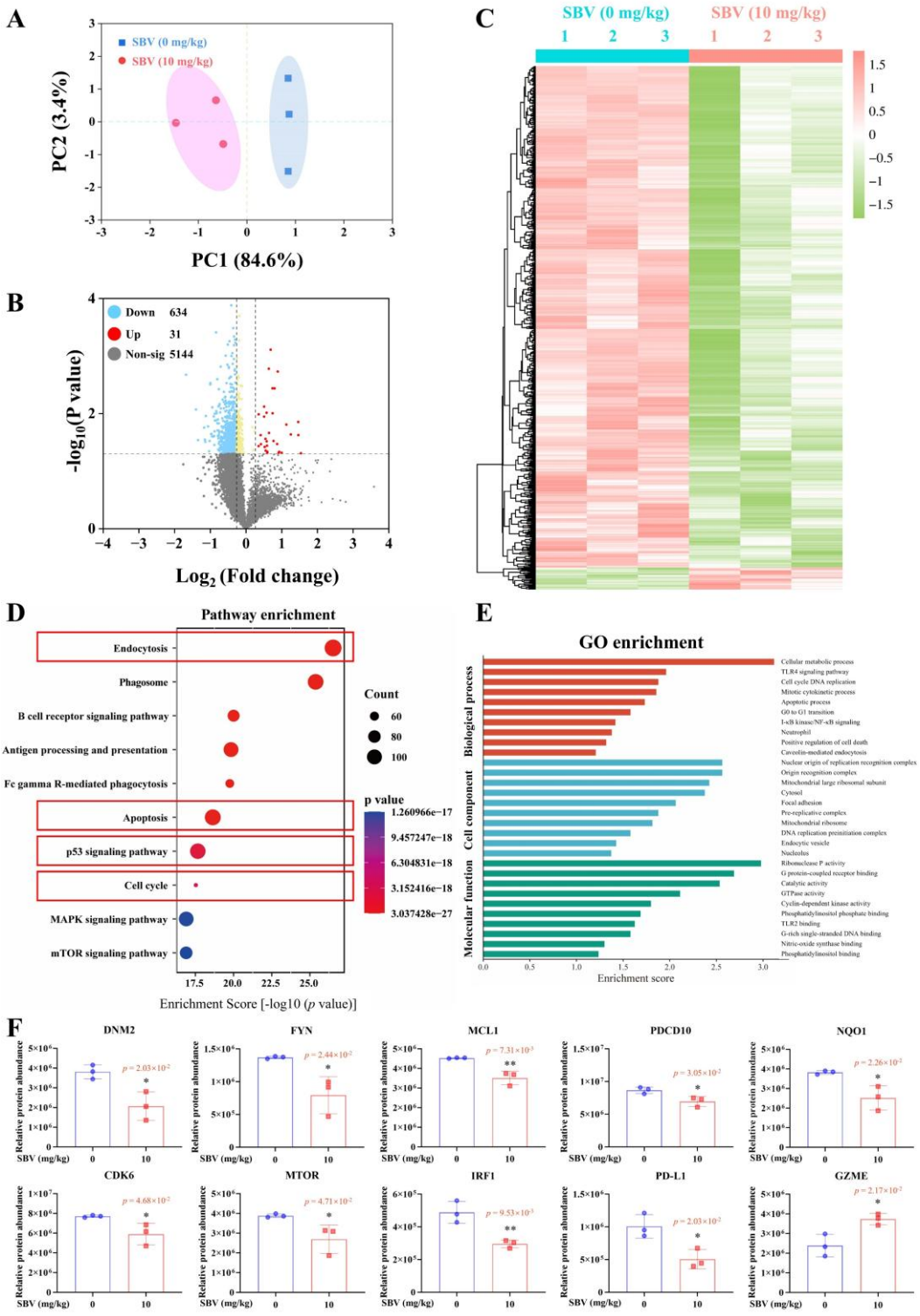

Figure 7. *In vivo* proteomic analysis of MC38 tumors from SBV-treated mice. (A) PCA score plot showing segregation between control and SBV (10 mg/kg) treated groups. **(B)** Volcano plot of DEPs identified in tumor tissues. Red dots represent 31 upregulated proteins, blue dots represent 634 downregulated proteins (|Fold Change| > 1.2, $p < 0.05$). **(C)** Hierarchical clustering heatmap of all DEPs. **(D)** KEGG pathway enrichment analysis of DEPs. **(E)** GO enrichment analysis of biological process, cell component and molecular function. **(F)** Validation of key DEPs involved in endocytosis, apoptosis, cell cycle, p53 signaling, and immune regulation related pathways. Data were shown as mean ± SD (n = 3); The normality of data was assessed using the Shapiro-Wilk test. Statistical significance between groups was determined by unpaired Student's t-test. *$p < 0.05$ and **$p < 0.01$ vs. control group.

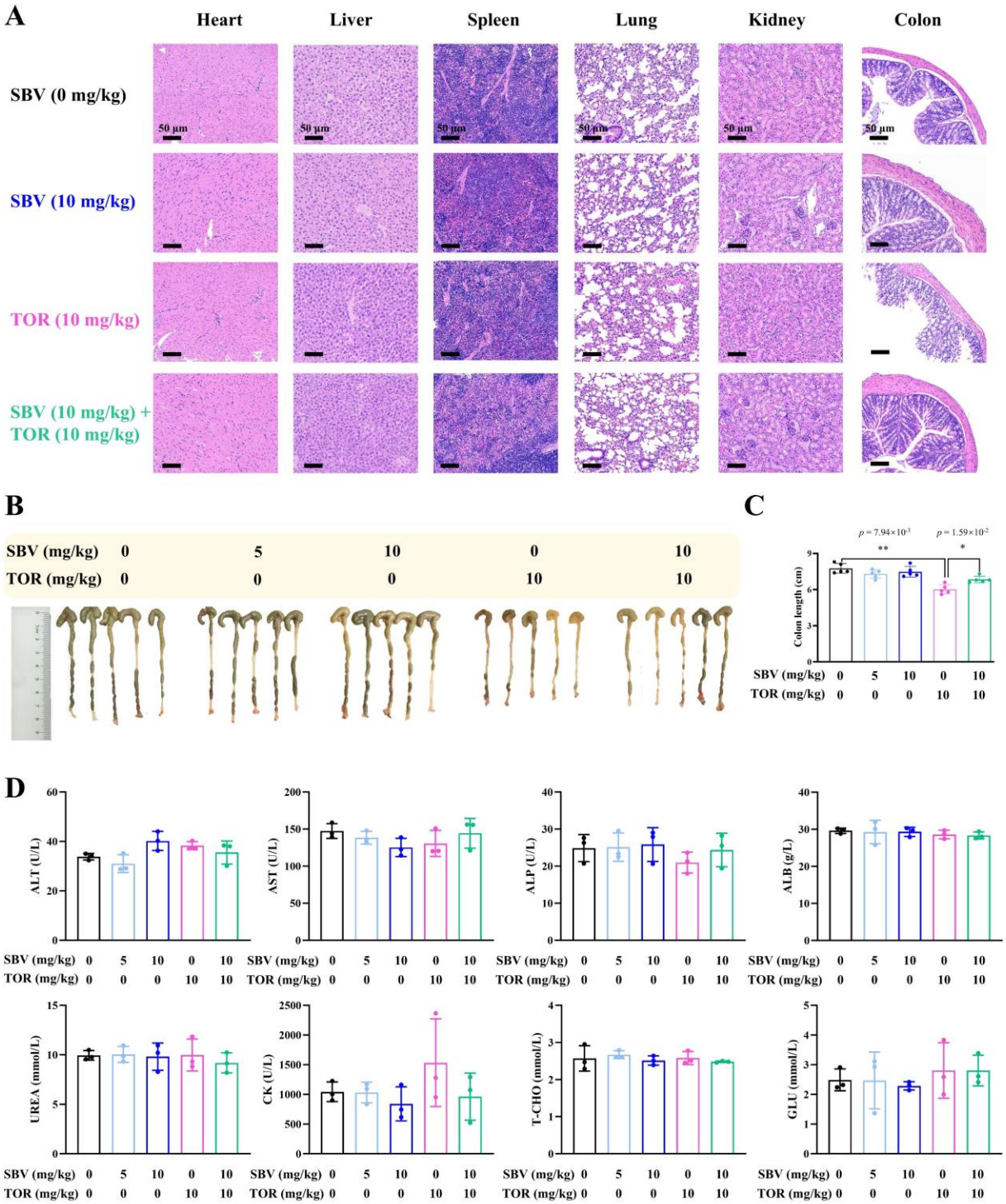

Figure 8. Biosafety evaluation of SBV *in vivo*. (A) H&E staining of major organs (heart, liver, spleen, lung, kidney, and colon) from mice in different treatment groups. Scale bar, 50 μm. **(B)** Representative image colon tissues showing the colonic morphology and mucosal architecture. **(C)** Statistical analysis of colon length across experimental groups. Data are shown as mean ± SD (n = 5). **(D)** Serum biochemical profiles assessing markers of systemic toxicity. Data are shown as mean ± SD (n = 3). Statistical significance was determined using non-parametric tests followed by Kruskal-Wallis with Dunn's multiple comparisons test. *$p < 0.05$ and **$p < 0.01$ vs. control or TOR group.

Proteomic alterations in MC38 xenograft tumor treated with SBV

To decipher the *in vivo* molecular mechanisms of SBV, we ran a quantitative proteomic analysis on MC38 xenograft tumors from SBV (10 mg/kg) and control groups. PCA showed obvious separation between groups, having PC1 explain 84.6% out of the variance (Fig. 7A). We noted 665 DEPs (|Fold Change| > 1.2, $p < 0.05$), having 31 proteins being upregulated and 634 being downregulated (Fig. 7B). Unsupervised hierarchical clustering confirmed separate proteomic profiles between control and SBV-treated tumors (Fig. 7C). KEGG enrichment analysis suggested notable modifications in endocytosis, apoptosis, p53 signaling, and cell cycle pathways, consistent with *in vitro* data (Fig. 7D). GO analysis further interpreted the biological processes influenced by SBV (Fig. 7E). Some key DEPs showed significant downregulation among endocytosis-related proteins (DNM2 and FYN), apoptosis regulators (MCL1 and PDCD10), cell cycle promoters (CDK6 and MTOR), and immune-related proteins (IRF1 and PD-L1). In addition, SBV treatment up-regulated granzyme E (GZME) and diminished protumor protein (NQO1) (Fig. 7F).

Evaluation of SBV biosafety *in vivo*

Histopathological analysis of principal organs (heart, liver, spleen, lung, kidney, and colon) showed no significant morphological alterations or signs of toxicity in any treatment group (Fig. 8A). Tissue architecture and cellular integrity were on par with those in the vehicle control group, showing that SBV alone or in conjunction with TOR did not induce detectable organ damage. In colon tissue, groups treated with SBV at doses of 0, 5, and 10 mg/kg showed normal colon length and mucosal architecture. By comparison, TOR monotherapy resulted in distinct colon shortening, mucosal atrophy, and ulceration. In the combined group of SBV and TOR, these adverse effects were considerably diminished, presenting a restored crypt structure and increased integrity of the intestinal wall (Fig. 8A, 8B, and 8C). To further assess systemic toxicity, serum biochemical analysis was performed. Key markers of hepatocellular injury (ALT and AST), cholestasis and hepatic biosynthesis (ALP and ALB), renal filtration function (UREA), cardiac and skeletal muscle integrity (CK), and systemic metabolism (T-CHO, GLU). The results demonstrated no statistically significant differences in any of these parameters across the five experimental groups (Fig. 8D).

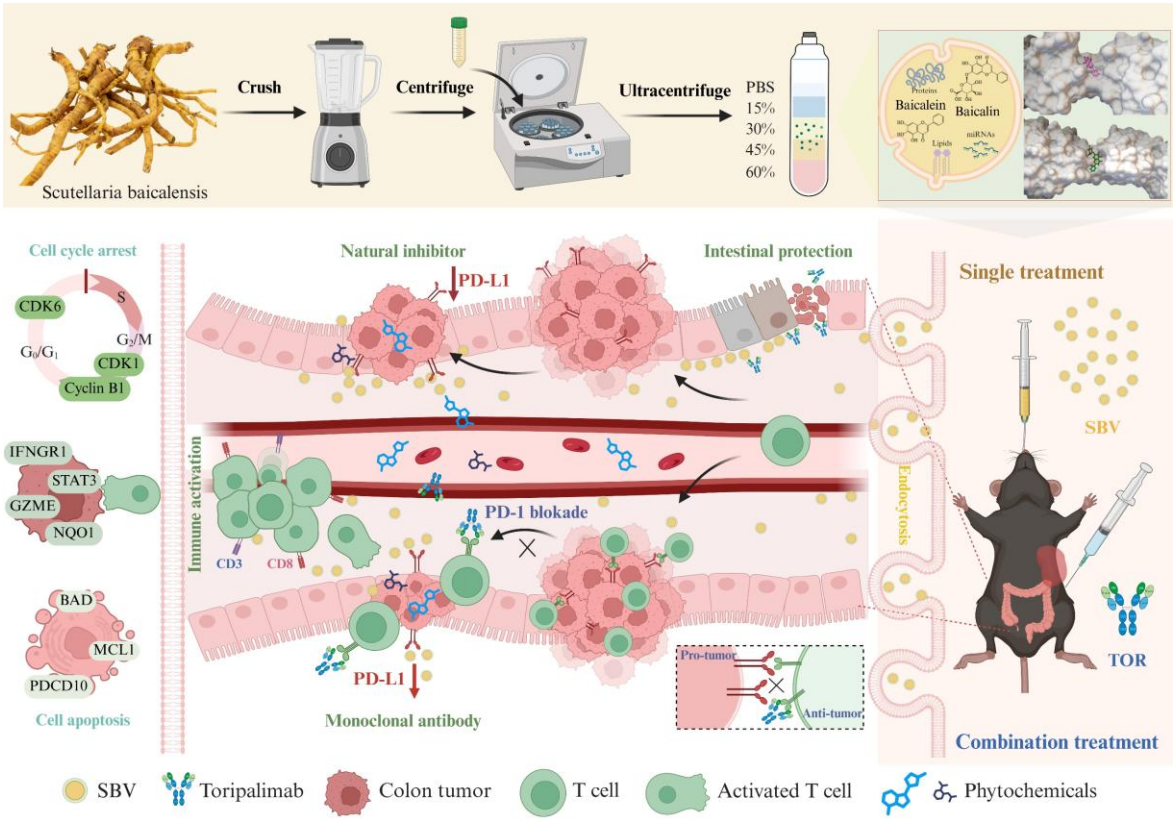

Figure 9. Mechanisms underlying the immunomodulatory effects of SBV against colorectal cancer. (Created in BioRender, agreement number: FF2982AKKO)

DISCUSSION

The PD-L1 plays a vital role in tumors evading host antitumor immune attack [35]. Its expression tethering interaction with PD-1 on T cells results in T-cell exhaustion and apoptosis. Because of such important functions, PD-L1 has been regarded as a primary target in oncology for reactivating antitumor immunity by therapeutic interventions [36]. Previous research has revealed that classes of natural compounds, including baicalein and baicalin from *Scutellaria baicalensis*, are capable of tethering expression of PD-L1 and modulating system immunity [29, 37]. Based on these findings, we hypothesized that SBV may also exhibit immunomodulatory effects via inhibition of PD-L1. To comprehensively assess this notion, we employed an integrated strategy involving molecular docking, western blotting, flow cytometry, and proteomic analysis both *in vitro* and *in vivo*. Our initial molecular docking studies reveal a high probability for constituents in SBV directly binding to PD-L1. We hypothesized that this direct binding event was not simply a physical blockade of protein-protein interaction but instead the priming event that facilitated subsequent downregulation and proteolytic degradation of PD-L1 protein. Consistently, our *in vitro* and *in vivo* data revealed that SBV treatment significantly suppressed PD-L1 expression.

In addition to PD-L1 regulation, integrated proteomic analyses *in vitro* and *in vivo* delineate the multi-targeted mechanism of SBV exerting anti-colorectal cancer activity. Specifically, the significant upregulation of p53 signaling-related proteins (PIG3 and ATM) indicated activation of DNA damage response and pro-apoptotic pathways. *In vitro*, the significant upregulation of p53 signaling components (PIG3 and ATM) indicating activation of DNA damage response and pro-apoptotic mechanisms [38]. Meanwhile, the downregulation of CDK1 and Cyclin B1 suggested G2/M cell cycle arrest [39]. Additionally, the modulation of anti-apoptotic proteins, including downregulation of MCL1 and BAD, indicated the rebalancing of apoptotic threshold toward cell death [40, 41]. Importantly, the consistent downregulation of PD-L1 and upstream signaling related proteins (IFGR1 and STAT3) in cellular proteomics and GO enrichment terms of "T cell receptor binding" and "positive regulation of T cell mediated immunity", provided a molecular basis for the immunostimulatory effect of SBV [42, 43]. Interestingly, these findings were further recapitulated *in vivo* tumor proteomic analysis, indicating SBV regulated p53 signaling, endocytosis, cell cycle, apoptosis, and immune pathways. Downregulation of DNM2 and FYN (involved in endocytosis and oncogenic signaling) [44, 45], MCL1 and PDCD10 (anti-apoptotic proteins [46, 47] , CDK6 and MTOR (cell cycle and growth regulators [48, 49], as well as IRF1 and PD-L1 (immune regulators [50, 51] , offer an integrated and validated model of the mechanism of SBV. The consistent downregulation of PD-L1 in both models as well as downregulation of several oncoproteins and activation of cytotoxic T cells strengthen the notion that SBV represents a novel, multi-targeted natural nanomedicine for colorectal cancer therapy. The downregulation of PD-L1, coupled with the modulation of p53 signaling and cell cycle progression, generates a favorable landscape for immune-mediated tumor control. The observed increase in $CD3^+$ and $CD8^+$ T cell population, along with upregulation of granzyme E (GZME)-a key effector molecule released by cytotoxic T cells to execute tumor cell killing [52]. Notably, simultaneous downregulation of protumor proteins such as NQO1 (mediated oxidative stress resistance and proliferation) by SBV indicates that SBV interferes with several oncogenic pathways to create an environment permissive for immune-mediated tumor clearance [53]. Collectively, integrated *in vitro* and *in vivo* proteomic data demonstrate that SBV exerts anti-tumor effect by coordinated mechanisms including inducing p53-mediated apoptosis and cell cycle arrest, while enhancing tumor immunity.

As shown in the cellular uptake experiments, the "endocytosis" pathway is an important route for SBV internalization [54]. Moreover, there was a positive correlation between uptake efficiency and therapeutic response. That is, the markedly higher internalization rate of SBV in MC38 cells than that in HT-29 cells was consistent with the higher sensitivity of MC38 cells to SBV internalization, as indicated by a lower IC_{50} value. These results suggested that the differences in SBV efficacy among colorectal cancer cell lines might be partially due to differences in endocytic capacity. MC38 cells had higher SBV internalization capability, which enhanced the downstream antitumor effects. In addition, the upregulation of ARRB2, which plays a pivotal role in the regulation of clathrin-mediated endocytosis, may facilitate SBV entry via enhancing the internalization activity of clathrin-dependent endocytosis [55].

PDV exhibit low toxicity and high biosafety in research models [56]. Compared with their monomeric parent compounds, PDV can reduce the drug dose while achieving the active component delivery to the tumor site [57]. In our study, SBV also exhibited excellent biosafety. Previous reports have shown that when TOR monotherapy was used in clinical, severe intestinal injury was induced, which is a well-known adverse reaction of immune checkpoint inhibitors [58]. Immune-related colitis and diarrhea were frequently observed in clinical trials in various cancer types and were listed as important adverse reactions in the prescribing information of TOR [59, 60]. Compared to previous reported PDV, SBV not

only enhanced the effect of TOR but also reduced the side effects of TOR therapy, thereby widening the therapeutic window of immune checkpoint blockade in colorectal cancer treatment. The above gut-protective properties may be since the components of *Scutellaria baicalensis* have an inherent anti-inflammatory activity, and the PDV have natural biocompatibility.

This study provides comprehensive evidence that SBV functions as a multifaceted nanotherapeutic platform against colorectal cancer through coordinated regulation of PD-L1 expression and multiple oncogenic pathways. Our findings demonstrate that SBV not only directly targets the PD-1/PD-L1 immune checkpoint axis but also orchestrates a broad antitumor response through modulation of key signaling pathways identified by proteomic analysis. While we have shown that SBV delivers bioactive flavonoids such as baicalin and baicalein, other vesicular cargos (including miRNAs, proteins, and lipids) may also contribute to its overall antitumor activity. Future studies will focus on deciphering the effects of these cargoes to illustrate the holistic mechanism of SBV.

Conclusions

Our study elucidates that SBV, as a natural nanoplatform, orchestrates a coordinated antitumor response by simultaneously inducing tumor-intrinsic effects (cell cycle arrest and apoptosis) and empowering tumor-extrinsic immunity (PD-L1 downregulation and T cell activation). The convergence of these pathways effectively switches the TME from immunosuppressive to immunostimulatory (Fig. 9). Given its efficacy and favorable safety profile, SBV represents a promising candidate for further development as a novel immunotherapeutic agent, either alone or in combination with existing regimens, for the treatment of colorectal cancer.

Acknowledgements

This study was supported by the Macao Science and Technology Development Fund (FDCT 0047/2025/ITP1, 0123/2022/A, 0008/2023/RIC, and 001/2023/ALC), the Research Fund of University of Macau (MYRG-GRG2023-00198-ICMS and SRG2022-00052-ICMS), and the Research Fund of Zhongzhi Pharmaceutical Group (CP-031-2023). We also appreciate the great assistance of Dr. TAN Wen from Lanzhou University and Dr. LIU Jingxin from Shenzhen Technology University in supporting this work.

Data availability

All data in this study are available by reasonable request.

Ethics approval and consent to participate

The animal experiments were approved by the Animal Ethics Committee of Zhuhai UM Science & Technology Research Institute (Approval No. ZUMRI-ERAE-013-2024) and were conducted in accordance with the National Institutes of Health (NIH) Guide for the Care and Use of Laboratory Animals.

Competing interests

The authors declare no competing financial or personal interests in this work.

Author contributions

Dianxin Cui: Writing-original draft, Validation, Methodology, Data curation, Investigation. Weilin Qiao: Conceptualization, Funding acquisition. Weixuan Chen: Resources, Methodology. Peng Li: Writing-review & editing, Funding acquisition. Shengpeng Wang: Formal analysis, Writing-review & editing. Fengyun Liao: Methodology, Data curation. Fei Li: Writing-review & editing, Kewei Wang: Writing-review & editing, Yitao Wang: Supervision, Funding acquisition. Huanxing Su: Formal analysis, Writing-review & editing Zhangfeng Zhong: Writing-review & editing, Conceptualization, Supervision, Funding acquisition.,

References

[1] Fenis A, Demaria O, Gauthier L, Vivier E, Narni-Mancinelli E (2024). New immune cell engagers for cancer immunotherapy. Nature Reviews Immunology, 24:471-486.

[2] Tufail M, Jiang C-H, Li N (2025). Immune evasion in cancer: mechanisms and cutting-edge therapeutic approaches. Signal Transduction and Targeted Therapy, 10:227.

[3] Zhang L, Lin Y, Hu L, Wang Y, Hu C, Shangguan X, et al. (2025). Transient intracellular expression of PD-L1 and VEGFR2 bispecific nanobody in cancer cells inspires long-term T cell activation and infiltration to combat tumor and inhibit cancer metastasis. Molecular Cancer, 24:119.

[4] Chen M, Su Z, Xue J (2025). Targeting T-cell Aging to Remodel the Aging Immune System and Revitalize Geriatric Immunotherapy. Aging Dis, 17:607-624.

[5] Siegel RL, Kratzer TB, Giaquinto AN, Sung H, Jemal A (2025). Cancer statistics, 2025. Ca-a Cancer Journal for Clinicians, 75:10-45.

[6] Wang F, Jin Y, Wang M, Luo HY, Fang WJ, Wang YN, et al. (2024). Combined anti-PD-1, HDAC inhibitor and anti-VEGF for MSS/pMMR colorectal cancer: a

randomized phase 2 trial. Nature Medicine, 30:1035-1043.

[7] Li JX, Wu C, Hu HB, Qin G, Wu XQ, Bai F, et al. (2023). Remodeling of the immune and stromal cell compartment by PD-1 blockade in mismatch repair-deficient colorectal cancer. Cancer Cell, 41:1152-1169.

[8] Cui D, Zhang C, Zhang L, Zheng J, Wang J, He L, et al. (2025). Natural anti-cancer products: insights from herbal medicine. Chinese Medicine, 20:82.

[9] Zheng W, Chen J, Liu J, Han X, Zhang S, Yang C, et al. (2025). Unveiling the potential of natural TLR modulators in cancer immunotherapy. Pharmacol Res, 221:107969.

[10] Huang J, Shi R, Chen F, Tan HY, Zheng J, Wang N, et al. (2024). Exploring the anti-hepatocellular carcinoma effects of Xianglian Pill: Integrating network pharmacology and RNA sequencing via in silico and in vitro studies. Phytomedicine, 133:155905.

[11] Liang Z, Wei J, Chan S, Zhang S, Xu L, Shen C, et al. (2025). Pinelliae Rhizoma: a systematic review on botany, ethnopharmacology, phytochemistry, preclinical and clinical evidence. Chin J Nat Med, 23:1-20.

[12] Xu Q, Jiang Z, Pan Y, Li S, Cao Z, Hua S, et al. (2025). Cucurbitacin B stimulates PD-1 immunotherapy response in malignant breast cancer by covalent targeting MTCH2. Phytomedicine, 145:157017.

[13] Takemoto M, Delghandi S, Abo M, Yurimoto K, Odagi M, Singh VP, et al. (2025). Covalent Plant Natural Product that Potentiates Antitumor Immunity. Journal of the American Chemical Society, 147:2902-2912.

[14] Zhong Z, Vong CT, Chen F, Tan H, Zhang C, Wang N, et al. (2022). Immunomodulatory potential of natural products from herbal medicines as immune checkpoints inhibitors: Helping to fight against cancer via multiple targets. Med Res Rev, 42:1246-1279.

[15] Xia J, Xu M, Hu H, Zhang Q, Yu D, Cai M, et al. (2024). 5,7,4'-Trimethoxyflavone triggers cancer cell PD-L1 ubiquitin-proteasome degradation and facilitates antitumor immunity by targeting HRD1. MedComm, 5:e611.

[16] Wang Q, Wang J, Yu D, Zhang Q, Hu H, Xu M, et al. (2024). Benzosceptrin C induces lysosomal degradation of PD-L1 and promotes antitumor immunity by targeting DHHC3. Cell Reports Medicine, 5:101357.

[17] Han XT, Zheng WY, Sun ZJ, Luo T, Li ZY, Lai WH, et al. (2025). Plant-derived exosomes: Unveiling the similarities and disparities between conventional extract and innovative form. Phytomedicine, 145:157087.

[18] Yi G, Luo H, Zheng Y, Liu W, Wang D, Zhang Y (2025). Exosomal Proteomics: Unveiling Novel Insights into Lung Cancer. Aging and Disease, 16:876-900.

[19] Song YY, Feng NA, Yu QY, Li YY, Meng MK, Yang X, et al. (2025). Exosomes in Disease Therapy: Plant-Derived Exosome-Like Nanoparticles Current Status, Challenges, and Future Prospects. International Journal of Nanomedicine, 20:10613-10644.

[20] Teng Y, Luo C, Qiu XL, Mu JY, Sriwastva MK, Xu QB, et al. (2025). Plant-nanoparticles enhance anti-PD-L1 efficacy by shaping human commensal microbiota metabolites. Nature Communications, 16:1295.

[21] Yang M, Guo J, Li J, Wang S, Sun Y, Liu Y, et al. (2025). Platycodon grandiflorum-derived extracellular vesicles suppress triple-negative breast cancer growth by reversing the immunosuppressive tumor microenvironment and modulating the gut microbiota. Journal of Nanobiotechnology, 23:92.

[22] Xu JL, Yu Y, Zhang Y, Dai HX, Yang QY, Wang BL, et al. (2024). Oral administration of garlic-derived nanoparticles improves cancer immunotherapy by inducing intestinal IFNγ-producing γδ T cells. Nature Nanotechnology, 19:1569-1578.

[23] Yan G, Xiao QY, Zhao JY, Chen HR, Xu Y, Tan MH, et al. (2024). Brucea javanica derived exosome-like nanovesicles deliver miRNAs for cancer therapy. Journal of Controlled Release, 367:425-440.

[24] Yang X, Zheng S, Wang X, Wang J, Ali Shah SB, Wang Y, et al. (2024). Advances in pharmacology, biosynthesis, and metabolic engineering of Scutellaria-specialized metabolites. Critical Reviews in Biotechnology, 44:302-318.

[25] Zhang J, Tan B, Wu H, Han T, Fang D, Cai H, et al. (2025). Scutellaria baicalensis Extracts Restrict Intestinal Epithelial Cell Ferroptosis by Regulating Lipid Peroxidation and GPX4/ACSL4 in Colitis. Phytomedicine, 141:156708.

[26] Gao Q, Sheng Q, Yang Z, Zhu Z, Li L, Xu L, et al. (2025). Honokiol-Magnolol-Baicalin Possesses Synergistic Anticancer Potential and Enhances the Efficacy of Anti-PD-1 Immunotherapy in Colorectal Cancer by Triggering GSDME-Dependent Pyroptosis. Advanced Science, 12:e2417022.

[27] Kong N, Chen X, Feng J, Duan T, Liu S, Sun X, et al. (2021). Baicalin induces ferroptosis in bladder cancer cells by downregulating FTH1. Acta Pharmaceutica Sinica B, 11:4045-4054.

[28] Li J, Zhang D, Wang S, Yu P, Sun J, Zhang Y, et al. (2025). Baicalein induces apoptosis by inhibiting the glutamine-mTOR metabolic pathway in lung cancer. Journal of Advanced Research, 68:341-357.

[29] Hao BJ, Lin SM, Liu HP, Xu JF, Chen L, Zheng TS, et al. (2025). Baicalein tethers CD274/PD-L1 for autophagic degradation to boost antitumor immunity. Autophagy, 21:917-933.

[30] Cui Y, Liu J, Wang X, Wu Y, Chang Y, Hu X, et al. (2025). Baicalin attenuates the immune escape of oral squamous cell carcinoma by reducing lactate accumulation in tumor microenvironment. Journal of Advanced Research, 77:721-732.

[31] Aliakbari F, Marzookian K, Parsafar S, Hourfar H, Nayeri Z, Fattahi A, et al. (2024). The impact of hUC MSC-derived exosome-nanoliposome hybrids on α-synuclein fibrillation and neurotoxicity. Science Advances, 10:eadl3406.

[32] Zhou M, Tang Y, Lu Y, Zhang T, Zhang S, Cai X, et al. (2025). Framework Nucleic Acid-Based and Neutrophil-Based Nanoplatform Loading Baicalin with

Targeted Drug Delivery for Anti-Inflammation Treatment. Acs Nano, 19:3455-3469.

[33] Shi R, Tan W, Jin H, Chan SI, Li W, Lei SS, et al. (2025). MicroRNA-Enriched Plant-Derived Exosomes Alleviate Colitis by Modulating Systemic Immunity, Metabolic Homeostasis, and Gut Microbiota. Advanced Science, 12:e05921.

[34] Liu H, Guo L, Zhang J, Zhou Y, Zhou J, Yao J, et al. (2019). Glycosylation-independent binding of monoclonal antibody toripalimab to FG loop of PD-1 for tumor immune checkpoint therapy. MABs, 11:681-690.

[35] Qin L, Liang T, Zhu X, Hu W, Li B, Wei M, et al. (2025). Senescent Macrophages and the Lung Cancer Microenvironment: A New Perspective on Tumor Immune Evasion. Aging Dis, 16:3453-3465.

[36] Huang Y, Chen C, Su M, Li D, Zhang J, Long K, et al. (2026). MCUB Inhibits PRKN-Dependent Mitophagic Degradation of PD-L1 to Promote Immune Evasion in Bladder Cancer. Adv Sci, 13: e14764.

[37] Zheng W, Chen J, Liu J, Han X, Zhang S, Yang C, et al. (2025). Unveiling the potential of natural TLR modulators in cancer immunotherapy. Pharmacological Research, 221:107969.

[38] Huang RX, Zhou PK (2020). DNA damage response signaling pathways and targets for radiotherapy sensitization in cancer. Signal Transduction and Targeted Therapy, 5:60.

[39] Lin L, Shen D, Su Y, Zhang Z, Yu J, Xu C, et al. (2025). Magnesium Lithospermate B Protects Against Ischemic AKI-to-CKD progression via regulating the KLF5/CDK1/Cyclin B1 pathway. Phytomedicine, 142:156765.

[40] Gui W, Paral P, Dhamija B, Hagag E, Dusa M, Humajova J, et al. (2025). MCL1 modulates mTORC1 signaling to promote bioenergetics and tumorigenesis. Nature Communications, 16:10841.

[41] Li Z, Ning K, Zhao D, Zhou Z, Zhao J, Long X, et al. (2023). Targeting the Metabolic Enzyme PGAM2 Overcomes Enzalutamide Resistance in Castration-Resistant Prostate Cancer by Inhibiting BCL2 Signaling. Cancer Research, 83:3753-3766.

[42] Song TL, Nairismägi ML, Laurensia Y, Lim JQ, Tan J, Li ZM, et al. (2018). Oncogenic activation of the STAT3 pathway drives PD-L1 expression in natural killer/T-cell lymphoma. Blood, 132:1146-1158.

[43] Yuan ZW, Yu TY, Wang X, Meng KL, Wang TL, Wang BY, et al. (2025). Glutamine deprivation confers immunotherapy resistance by inhibiting IFN-γ signaling in cancer cells. Pharmacological Research, 213:107643.

[44] Trochet D, Bitoun M (2021). A review of Dynamin 2 involvement in cancers highlights a promising therapeutic target. Journal of Experimental & Clinical Cancer Research, 40:238.

[45] Cabral-Dias R, Lucarelli S, Zak K, Rahmani S, Judge G, Abousawan J, et al. (2022). Fyn and TOM1L1 are recruited to clathrin-coated pits and regulate Akt signaling. Journal of Cell Biology, 221:e201808181.

[46] Vogler M, Braun Y, Smith VM, Westhoff MA, Pereira RS, Pieper NM, et al. (2025). The BCL2 family: from apoptosis mechanisms to new advances in targeted therapy. Signal Transduction and Targeted Therapy, 10:91.

[47] Valentino M, Dejana E, Malinverno M (2021). The multifaceted PDCD10/CCM3 gene. Genes & Diseases, 8:798-813.

[48] Wu XW, Yang XB, Xiong Y, Li RT, Ito T, Ahmed TA, et al. (2021). Distinct CDK6 complexes determine tumor cell response to CDK4/6 inhibitors and degraders. Nature Cancer, 2:429-443.

[49] Li RL, Wang RR, Wang XM, Lin L, Wang CC, Jian Q, et al. (2025). The antitumor effects of lupenone on colon cancer and its mechanistic insights. Phytomedicine, 145:156939.

[50] Wu Y, Zhou L, Zou Y, Zhang Y, Zhang M, Xu L, et al. (2023). Disrupting the phase separation of KAT8-IRF1 diminishes PD-L1 expression and promotes antitumor immunity. Nature Cancer, 4:382-400.

[51] Lin X, Kang K, Chen P, Zeng Z, Li G, Xiong W, et al. (2024). Regulatory mechanisms of PD-1/PD-L1 in cancers. Molecular Cancer, 23:108.

[52] Hu MD, Golovchenko NB, Burns GL, Nair PM, Kelly TJ, Agos J, et al. (2022). γδ Intraepithelial Lymphocytes Facilitate Pathological Epithelial Cell Shedding Via CD103-Mediated Granzyme Release. Gastroenterology, 162:877-889.

[53] Yuan ZN, Wang XY, Qin BY, Hu RL, Miao R, Zhou Y, et al. (2024). Targeting NQO1 induces ferroptosis and triggers anti-tumor immunity in immunotherapy-resistant KEAP1-deficient cancers. Drug Resistance Updates, 77:101160.

[54] Yin LF, Yan L, Yu Q, Wang J, Liu CH, Wang L, et al. (2022). Characterization of the MicroRNA Profile of Ginger Exosome-like Nanoparticles and Their Anti-Inflammatory Effects in Intestinal Caco-2 Cells. Journal of Agricultural and Food Chemistry, 70:4725-4734.

[55] Bae WY, Choi JS, Nam S, Jeong JW (2021). β-arrestin 2 stimulates degradation of HIF-1α and modulates tumor progression of glioblastoma. Cell Death and Differentiation, 28:3092-3104.

[56] Feng WJ, Teng YT, Zhong QP, Zhang YM, Zhang JW, Zhao P, et al. (2023). Biomimetic Grapefruit-Derived Extracellular Vesicles for Safe and Targeted Delivery of Sodium Thiosulfate against Vascular Calcification. Acs Nano, 17:24773-24789.

[57] Xu Y, Yan G, Zhao JY, Ren YH, Xiao QY, Tan MH, et al. (2024). Plant-derived exosomes as cell homogeneous nanoplatforms for brain biomacromolecules delivery ameliorate mitochondrial dysfunction against Parkinson's disease. Nano Today, 58:102438.

[58] Wang ZH, Wang XC, Zhang XY, Leng JH, Cui M, Zhang J, et al. (2025). Toripalimab, bevacizumab, and irinotecan in dMMR/MSI locally advanced colorectal cancer First-stage results from a phase 1b/2 trial. Cell Reports Medicine, 6:102296.

[59] Wang FH, Wei XL, Feng JF, Li Q, Xu N, Hu XC, et al. (2021). Efficacy, Safety, and Correlative Biomarkers of Toripalimab in Previously Treated Recurrent or Metastatic Nasopharyngeal Carcinoma: A Phase II Clinical Trial (POLARIS-02). Journal of Clinical Oncology, 39:704-712.

[60] Wang ZX, Cui CX, Yao J, Zhang YQ, Li MX, Feng JF, et al. (2022). Toripalimab plus chemotherapy in treatment-naive, advanced esophageal squamous cell carcinoma (JUPITER-06): A multi-center phase 3 trial. Cancer Cell, 40:277-288.